


**Dueling dynamical backaction in a cryogenic optomechanical cavity**

B. D. Hauer,<sup>\*</sup> T. J. Clark, P. H. Kim, C. Doolin, and J. P. Davis<sup>†</sup>  
*Department of Physics, University of Alberta, Edmonton, Alberta, Canada T6G 2E9*

 (Received 10 January 2019; published 2 May 2019)

Dynamical backaction has proven to be a versatile tool in cavity optomechanics, allowing for precise manipulation of a mechanical resonator's motion using confined optical photons. In this work, we present measurements of a silicon whispering-gallery-mode optomechanical cavity where backaction originates from opposing radiation-pressure and photothermal forces, with the former dictating the optomechanical spring effect and the latter governing the optomechanical damping. At high enough optical input powers, we show that the photothermal force drives the mechanical resonator into self-oscillations for a pump beam detuned to the low-frequency side of the optical resonance, contrary to what one would expect for a radiation-pressure-dominated optomechanical device. Using a fully nonlinear model, we fit the hysteretic response of the optomechanical cavity to extract its properties, demonstrating that this non-sideband-resolved device exists in a regime where photothermal damping could be used to cool its motion to the quantum ground state.

DOI: [10.1103/PhysRevA.99.053803](https://doi.org/10.1103/PhysRevA.99.053803)

**I. INTRODUCTION**

Over the past several years, the field of cavity optomechanics, which studies the interplay between the photonic modes of an optical cavity and the phononic modes of a mechanical resonator, has proven itself to be a tremendous resource. Along with numerous applications in precision metrology [1–4] and quantum information [5–7], optomechanical systems have also demonstrated potential in providing an experimental testbed to help answer a number of fundamental questions in quantum mechanics [8–11] and gravity [12–15]. One of the most powerful phenomena demonstrated by optomechanical systems, however, has been their ability to use photons confined within an optical cavity to manipulate the motion of a mechanical resonator via the radiation-pressure force. Using the delayed nature of this interaction, which arises due to the finite lifetime of the photons within in the cavity, the optical field is able to modify the properties of the mechanical resonator, resulting in dynamical backaction between the optical and mechanical modes of the system [16].

By detuning an optical pump to the lower-frequency (red) side of the optical cavity, energy can be extracted from the mechanical resonator via resonantly enhanced anti-Stokes scattering processes that preferentially promote detuned photons into the higher energy states of the optical cavity. The opposite process (Stokes scattering) will then occur for a pump detuned to the higher frequency (blue) side of the cavity, such that the photons instead provide energy to the mechanical element, thus amplifying its motion. Accompanying each of these dynamical backaction processes is an increase in the mechanical damping rate, or cooling of the resonator's motion, for a red-detuned optical pump, while for a blue-detuned pump, the damping rate decreases. This

process, known as optomechanical damping, is mirrored by the optomechanical spring effect, which in the non-sideband-resolved regime results in a decrease (increase) in the resonance frequency of the mechanical oscillator for a red (blue) detuned pump, such that these two dynamical backaction effects obey the Kramers-Kronig relations [17]. Employing these radiation-pressure-driven effects, a number of groundbreaking experiments have been performed using optomechanical cavities, including motional ground state cooling of micro/nanomechanical resonators [18,19], entanglement of photonic and phononic modes [20–22], and preparation of other nonclassical states of mechanical motion [6,23,24].

Though efforts have largely focused on this radiation-pressure-driven interaction, optomechanical coupling can be mediated by other means, such as the photothermal (or bolometric) force, whereby photon absorption in the mechanical element introduces a temperature gradient across the device, causing it to deflect due to differential thermal contractions [25–29]. Photothermal effects have historically been studied in optical cavities composed of metal-coated cantilevers [30–37], but have also been observed in buckled microcavities [38,39], multilayered Bragg-mirror beams [40,41], membranes [42–44], thin metallic mirrors [45], nanowires [38,46,47], split-ring resonators [48], and superfluid helium [49–51]. As in the case of radiation-pressure-driven optomechanics, photothermal forces can also be used to manipulate the motion of mechanical resonators. In fact, in a somewhat paradoxical sense, photothermal coupling can be used to cool a resonator's motion to occupancies of less than a single phonon on average [25–29]. Furthermore, photothermal dynamical backaction is peculiar in that it is able to invert the detuning dependence of the optomechanical damping (and spring effect) with respect to that found in conventional radiation-pressure-driven systems, where such a reversal is only possible for cavities that are externally driven to large mechanical amplitudes in the sideband-resolved regime [52–55]. In the

<sup>\*</sup>bhauer@ualberta.ca

<sup>†</sup>jdavis@ualberta.ca

non-sideband-resolved regime, however, this inversion effect results in amplification of the resonator's motion (accompanied by an increase in the mechanical resonance frequency) for red-detuned pumps, while cooling (along with a decrease in the mechanical resonance frequency) occurs for blue-detuned pumps [32–35,39,41,42], seemingly violating the conservation of energy. While there have been brief mentions of a radiation-pressure-dominated spring effect observed in photothermally driven optomechanical devices [32,33,35,41], to date there has not been a thorough experimental investigation of how the photothermal and radiation-pressure forces interact with each other. Therefore, a comprehensive study of this interaction is warranted, especially in the case of cryogenic silicon optomechanical cavities, as these devices are integral to a number of quantum optomechanical experiments [6,21,56–58].

In this article, we present and quantitatively analyze measurements of a silicon whispering-gallery-mode optomechanical cavity that exists in a parameter regime where both radiation-pressure and photothermal effects are relevant. We begin by providing a brief theoretical overview for a nonlinear optomechanical system that is subject to both of these forces. Applying this theory to the studied device, we find that radiation pressure dominates the optical spring effect, while photothermal interactions govern the system's optomechanical damping. Moreover, this photothermal force acts to oppose its radiation-pressure counterpart, such that the optomechanical damping has the opposite detuning-dependence from what one would expect for a conventional radiation-pressure-driven system, resulting in an oddly similar detuning-dependence between the optomechanical damping and spring effect. With this photothermal enhancement to the optomechanical damping, we find that for high enough optical input powers we are able to drive the mechanical resonator into self-oscillations using a red-detuned pump. We show that in this self-oscillating regime, the transmission through the optical cavity, as well as the optomechanical damping and spring effect, become highly nonlinear, while demonstrating hysteretic behavior depending on the sweep direction of the optical drive. Using our fully nonlinear model, we fit these data, extracting the optomechanical properties of the system. From these experimentally determined parameters, we assess the device's ability to cool the motion of the resonator using the photothermal effect for a blue-detuned optical pump. In doing so, we find that the mechanical occupancy can, in principle, be reduced to less than a single phonon on average, despite the fact that the optomechanical cavity resides deeply in the non-sideband-resolved regime.

## II. THEORETICAL MODEL

To describe the behavior of the device studied in this work, we consider an optomechanical system composed of an optical cavity, with resonant frequency  $\omega_c$  and total loss rate  $\kappa$ , coupled to a mechanical resonator, with a resonant frequency  $\omega_m$  and intrinsic damping rate  $\Gamma_m$ . We assume that a dispersive coupling exists between these two systems due to the fact that the displacement  $x$  of the mechanical oscillator shifts the resonance frequency of the optical cavity by an amount  $Gx$ , where  $G = -d\omega_c/dx$  is the dispersive

optomechanical coupling coefficient. For such a system, the coupled classical equations of motion will be given by [16,49]

$$\dot{a} = -\frac{\kappa}{2}a + i\Delta_0 a + iGxa + \sqrt{\kappa_e}\bar{a}_{\text{in}}, \quad (1)$$

$$\ddot{x} + \Gamma_m \dot{x} + \omega_m^2 x = \frac{1}{m}[F_{\text{th}} + F_{\text{rp}} + F_{\text{pt}}]. \quad (2)$$

Equation (1) describes the time evolution of the optical cavity's field amplitude  $a$ , which is driven by an input field  $\bar{a}_{\text{in}}$ . This drive field, whose strength is related to the input power  $P_{\text{in}}$  of the optical signal via the relation  $|\bar{a}_{\text{in}}|^2 = P_{\text{in}}/\hbar\omega_d$  [16], is coupled into the cavity at a rate  $\kappa_e$ , with its frequency  $\omega_d$  detuned from cavity resonance by an amount  $\Delta_0 = \omega_d - \omega_c$ . With this definition of detuning, negative (positive) values indicate a red-detuned (blue-detuned) cavity drive. Meanwhile, Eq. (2) governs the dynamics of the mechanical resonator's displacement, which is simultaneously driven by an intrinsic thermal force  $F_{\text{th}}$ , a radiation-pressure force  $F_{\text{rp}} = \hbar G|a|^2$  [16,49], and a photothermal force [25–29]

$$F_{\text{pt}}(t) = \frac{\hbar G\beta}{\tau} \int_{-\infty}^t e^{-\frac{t-t'}{\tau}} |a(t')|^2 dt'. \quad (3)$$

Here the dimensionless parameter  $\beta$  sets the relative strength of the photothermal force with respect to the radiation-pressure force and is heavily dependent on the optical and mechanical modes being considered [35,49], as well as the thermal properties of the resonator [28,29]. We further note that  $\beta$  can be negative, such that the photothermal force acts to directly oppose radiation-pressure effects [32–35,39,41,42], which has very important consequences for the detuning-dependence of the optomechanical damping and spring effects. Also included in Eq. (3) is the thermal relaxation time  $\tau$ , which sets the timescale of the photothermal force and, similar to  $\beta$ , is determined by the thermal properties and geometry of the device (see Appendix E). Finally, while we have chosen to explicitly identify Eq. (3) as being photothermal in nature, the following analysis is valid for any optomechanical force that has a delayed response with respect to the occupation of the optical cavity.

To solve Eqs. (1) and (2), we begin by assuming that for a high- $Q$  mechanical resonator ( $Q_m = \omega_m/\Gamma_m \gg 1$ ) driven to a large amplitude of motion, the mechanical displacement will be well-described by the ansatz  $x(t) = \bar{x} + A \cos(\omega_m t)$ , where  $\bar{x}$  and  $A$  are the resonator's static shift in displacement and amplitude of oscillation, respectively [16,52,53]. Inputting this ansatz into Eq. (1), we find

$$a(t) = \sqrt{\kappa_e}\bar{a}_{\text{in}}e^{i\phi(t)} \sum_{k=-\infty}^{\infty} \alpha_k e^{ik\omega_m t}, \quad (4)$$

with  $\phi(t) = \xi \sin(\omega_m t)$  being the time-dependent global phase of the optical field and

$$\alpha_k = \frac{J_k(-\xi)}{\kappa/2 - i(\Delta_0 + G\bar{x} - k\omega_m)}, \quad (5)$$

where  $J_k(z)$  is the  $k$ th Bessel function of the first kind and  $\xi = GA/\omega_m$  is the dimensionless mechanical modulation strength [16,52–54,59]. Using these solutions for  $x(t)$  and  $a(t)$ , the mechanical-amplitude-dependent

optomechanical spring effect  $\delta\omega_m$  and damping  $\delta\Gamma_m$  are found to be (see Appendix B)

$$\delta\omega_m = -\frac{\hbar G\kappa_e |\bar{a}_{in}|^2}{Am\omega_m} \sum_{k=-\infty}^{\infty} \text{Re} \left\{ \alpha_k \alpha_{k+1}^* \left( 1 + \frac{\beta}{1 - i\omega_m \tau} \right) \right\}, \quad (6)$$

$$\delta\Gamma_m = \frac{2\hbar G\kappa_e |\bar{a}_{in}|^2}{Am\omega_m} \sum_{k=-\infty}^{\infty} \text{Im} \left\{ \alpha_k \alpha_{k+1}^* \left( 1 + \frac{\beta}{1 - i\omega_m \tau} \right) \right\}, \quad (7)$$

from which we can find the total mechanical damping rate as  $\Gamma_{\text{tot}} = \Gamma_m + \delta\Gamma_m$ . Finally, using Eq. (4), along with the input-output relation  $\bar{a}_{\text{out}} = \bar{a}_{\text{in}} - \sqrt{\kappa_e} a$ , we can also determine the transmission through the optical cavity as [16,59]

$$\mathcal{T} = \frac{|\bar{a}_{\text{out}}|^2}{|\bar{a}_{\text{in}}|^2} = 1 - 2\kappa_e \text{Re} \left\{ \sum_{k=-\infty}^{\infty} J_{-k}(\xi) \alpha_k \right\} + \kappa_e^2 \sum_{k=-\infty}^{\infty} |\alpha_k|^2. \quad (8)$$

We note that by taking the small mechanical amplitude limit (i.e.,  $\xi \ll 1$ ) for each of the quantities in Eqs. (6), (7), and (8), their standard linearized expressions can be obtained (see Appendix B).

The two expressions in Eqs. (6) and (7) resemble what one would expect for a radiation-pressure-driven optomechanical system that has been driven to large mechanical amplitude, with the addition of the  $\beta/(1 - i\omega_m \tau)$  term to account for the photothermal interaction [52]. Photothermal forces will therefore govern these dynamical backaction effects when this additional term overwhelms its radiation-pressure counterpart (see Appendix B). For a non-sideband-resolved optomechanical cavity, this occurs for the spring effect when

$$1 + \omega_m^2 \tau^2 \lesssim |\beta|, \quad (9)$$

and for the optomechanical damping when

$$1 + \omega_m^2 \tau^2 \lesssim \frac{|\beta| \kappa \tau}{2}. \quad (10)$$

Note the difference of  $\kappa \tau/2$  between Eqs. (9) and (10), as this factor quantifies the ratio of the photothermal time constant  $\tau$  to the cavity photon lifetime  $\tau_c = 1/\kappa$  (i.e., the relevant time scales associated with each optical force) and is significant in determining which force dominates the optomechanical damping [33,41]. This is especially true for non-sideband-resolved optomechanical cavities, where  $\kappa \tau$  tends to be large and photothermal damping effects are generally stronger than those found in sideband-resolved systems [25,26,28,29].

In Fig. 1, we investigate three different optomechanical regimes according to Eqs. (9) and (10). Interestingly, we find that there exists a parameter space where  $|\beta| < 1 + \omega_m^2 \tau^2$ , such that the spring effect is dominated by the radiation-pressure interaction, but  $\kappa \tau$  is large enough that Eq. (10) is satisfied and optomechanical damping is governed by the photothermal force. This parameter space is particularly interesting in the case where  $\beta$  is negative, resulting in the bizarre effect of a qualitatively similar detuning dependence between the optomechanical damping and spring effect, as

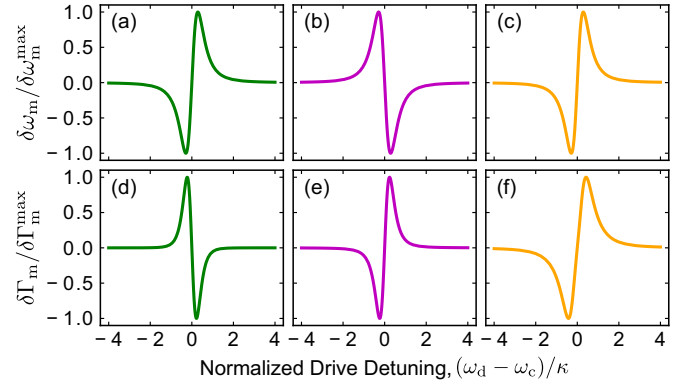


FIG. 1. Plots of the optomechanical (a)–(c) spring effect and (d)–(f) damping, normalized to their respective maximum values,  $\delta\omega_m^{\text{max}}$  and  $\delta\Gamma_m^{\text{max}}$ . Here we consider the small mechanical amplitude regime with both radiation-pressure and photothermal effects included [i.e., Eqs. (6) and (7) in the limit  $\xi \ll 1$ —see Appendix B], where we have taken (a, d)  $\beta = -0.1$ ,  $\omega_m \tau = 0.01$ , (b, e)  $\beta = -10$ ,  $\omega_m \tau = 0.01$ , and (c, f)  $\beta = -0.1$ ,  $\omega_m \tau = 1$ ; with  $\kappa/\omega_m = 100$  in all plots. Therefore, according to Eqs. (9) and (10), in (a, d) radiation pressure dominates both the spring effect and damping, while in (b, e) dynamical backaction is driven by photothermal forces. Finally, in (c, f) we enter into the dueling regime studied in this work, where the spring effect is dominated by the radiation-pressure force, while the optomechanical damping is governed by photothermal effects.

seen in Figs. 1(c) and 1(f). It is this regime, which we refer to as the “dueling regime,” that we investigate experimentally in the remainder of the paper.

### III. EXPERIMENT

The optomechanical device studied in this work is composed of a “clawlike” mechanical resonator that surrounds one quarter of the circumference of a 10- $\mu\text{m}$ -diameter microdisk (see Fig. 2). Both elements are fabricated from the 250-nm-thick single-crystal silicon device layer of a standard

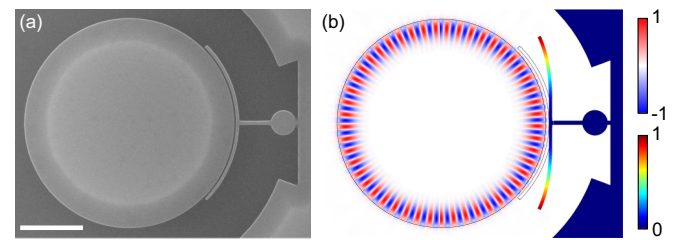


FIG. 2. (a) A scanning electron microscope image of the device studied in this work. Scale bar is 3  $\mu\text{m}$  (see Appendix A for detailed device dimensions). (b) Finite element method simulations of the normalized radial electric field magnitude for the first-order radial whispering-gallery mode of the disk with azimuthal mode number  $M = 49$ . Colors indicate the direction of the in-plane electric field, with blue/negative (red/positive) corresponding to an inward (outward) facing field with respect to the center of the disk. Also included is a finite element method simulation of the in-plane flexural crab mode of the mechanical resonator with the normalized displacement expressed in rainbow scale. Both mechanical and optical simulations are for the device in (a).

silicon-on-insulator chip (fabrication details can be found elsewhere [4]). The microdisk supports whispering-gallery-mode resonances in the telecom band, while the mechanical element exhibits a number of MHz-frequency flexural and torsional modes [see Fig. 2(b), for example]. For this device geometry, dispersive coupling arises between the optical and mechanical modes of the system due to the fact that the resonator’s motion through the evanescent field surrounding the microdisk acts to modulate its effective index, and therefore, its optical resonance frequencies. In this work, we focus on the in-plane flexural “crab” mode of the mechanical resonator [see Fig. 2(b)] with a measured resonant frequency of  $\omega_m/2\pi = 11.2$  MHz, as this mode traverses the steepest gradient of the optical field profile, resulting in a large dispersive optomechanical coupling quantified by  $G/2\pi = 0.817$  GHz/nm. Using the measured dimensions of the mechanical resonator (see Appendix A), along with its simulated modeshape, we find the effective motional mass of this mode to be  $m = 183$  fg [60], allowing us to determine its zero-point fluctuation amplitude as  $x_{zpf} = \sqrt{\hbar/2m\omega_m} = 64$  fm.

All measurements are performed inside a cryostat using a custom-built cryogenic optomechanical coupling apparatus [61], with exchange gas added to the vacuum can to promote thermalization of the device to the helium bath temperature of 4.2 K. Using this setup, laser light is directly injected into, and collected from, the optical cavity via a cryogenic dimpled-tapered fiber [62–64]. The transmission through the optical cavity is then monitored by directly observing the laser fluence through the fiber using a photodetector, while fluctuations in the optical signal are either transduced directly using this photodetector, or by switching out to a homodyne detection system (see Appendix A for details). This setup allows the advantage of being able to measure the mechanical signal using both direct and homodyne detection, as these two schemes are complimentary in a sense that one’s response will be maximized for detunings at which the other is minimized, providing optimal signal-to-noise in the transduced signal over the entire sweep of the optical resonance.

#### IV. RESULTS

In Fig. 3, we show measurements of the studied optomechanical system from two separate optical resonances with center wavelengths located at 1582 nm [Fig. 3(a)] and 1608 nm [Fig. 3(b)]. Here the optical resonance at 1582 nm exhibits the behavior one would expect for a standard radiation-pressure-driven optomechanical system [see Figs. 1(a) and 1(d)], where we observe optomechanical damping on the red side of the optical cavity and amplification on the blue side, with the mechanical spring effect exhibiting the opposite detuning dependence. However, this is not the case for the optical resonance at 1608 nm. Instead, the optomechanical damping behaves quite differently, with amplification on the red side of the optical cavity and damping on the blue side. Furthermore, the spring effect seems to qualitatively follow the same detuning dependence as the optomechanical damping, such that these two dynamical backaction effects appear to violate the Kramers-Kronig relations [17]. We note that this reversal in the detuning dependence of the optome-

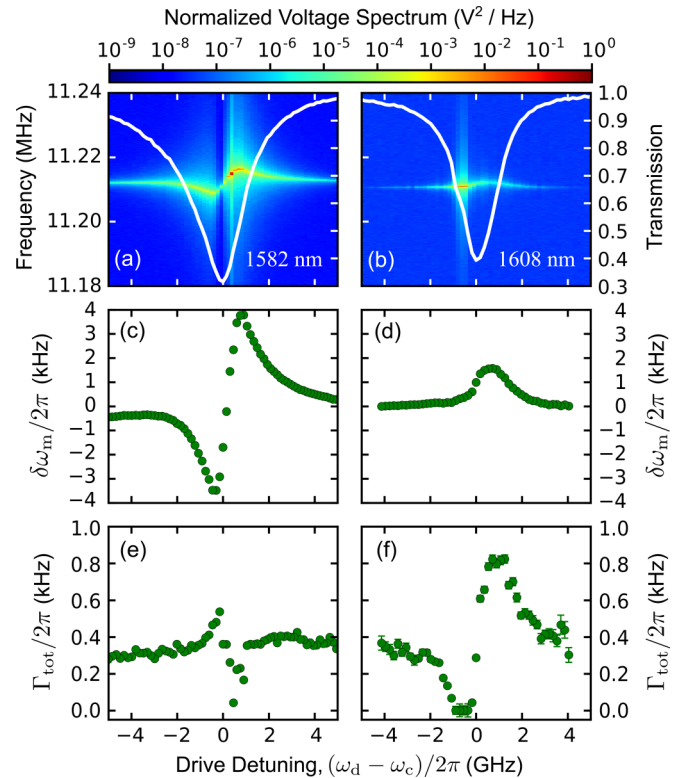


FIG. 3. Mechanical spectra (normalized to their maximum values) versus detuning for the 11.2 MHz crab mode depicted in Fig. 2(b) transduced using optical resonances at (a)  $\lambda_c = 1582$  nm and (b)  $\lambda_c = 1608$  nm, with the mechanical frequency on the left axis. Overlaid in white is the transmission through the cavity (right axis) for each optical mode. Note that while in (a) mechanical damping (amplification) occurs on the red (blue) side of the optical resonance, this effect is reversed in (b). Also included are (c, d) the optomechanical spring effect  $\delta\omega_m$  and (e, f) the total mechanical damping rate  $\Gamma_{\text{tot}} = \Gamma_m + \delta\Gamma_m$ , with (c) and (e) corresponding to the mechanical data in (a), while (d) and (f) are extracted from the data in (b). We attribute the lack of spring effect on the red side of the optical resonance in (d) to an optical-heating-induced mechanical frequency shift that offsets dynamical backaction effects [42]. Measurements are taken at input optical powers to the cavity of (a, c, e)  $P_{\text{in}} = 10.9 \mu\text{W}$  and (b, d, f)  $P_{\text{in}} = 1.9 \mu\text{W}$ , chosen such that self-oscillation of the mechanical motion has just begun to onset for each optical mode.

chanical damping is observed at optical input powers down to 50 nW (see Appendix D), indicating that this seemingly anomalous effect does not onset at a given power threshold. We attribute this behavior to an additional photothermal force that is present for the 1608 nm optical mode, with  $\beta$  and  $\tau$  satisfying  $\beta < 0$  and Eq. (10), but not Eq. (9), such that this force acts to overwhelm the device’s radiation-pressure-driven optomechanical damping, but not its spring effect. We postulate that photothermal effects arise in this optomechanical device for optical modes that heat the inner surface of the mechanical resonator (facing the disk) via optical absorption. This process in turn generates a thermal gradient across the width of the curved portion of the resonator, inducing thermoelastic forces that cause it to curl [42,43], thus actuating the crab mode.

The inverted detuning dependence associated with this effect becomes more pronounced at higher optical input powers, where we further find that the observed photothermal amplification is strong enough to reduce the total mechanical damping to zero, inducing a parametric instability in the system [52,53]. This causes the device to self-oscillate for a near-resonant red-detuned optical pump, driving the mechanical resonator's motion to amplitudes as large as  $A_{\max} = 5.2 \text{ nm}$  [=  $382 \omega_m/G$ —see Fig. 4(e)], nearly three orders of magnitude greater than its thermally driven amplitude of  $A_{\text{th}} = \sqrt{2k_B T/m\omega_m^2} = 11.3 \text{ pm}$  at  $T = 4.2 \text{ K}$ . Accompanying this increase in mechanical amplitude, we also observe highly nonlinear behavior in each of the spring effect, optomechanical damping, and transmission through the optical cavity (see Fig. 4), as well as a hysteresis in each of these quantities with respect to the sweep direction of the optical drive. We note that while the optomechanical interaction causing the device to enter into self-oscillation is nonlinear, the mechanical motion itself still remains within the linear regime, avoiding complications such as Duffing nonlinearities [65].

This peculiar behavior can be understood by examining the combined photothermal and radiation-pressure attractor diagram of the system [34,52–55], which is generated by evaluating Eq. (7) at various mechanical amplitudes  $A$  and optical drive detunings  $\Delta = \Delta_0 + G\bar{x}$  [see Fig. 4(e)]. Note that with this definition of  $\Delta$ , we include the shift in the cavity resonance due to the static, optomechanically induced displacement of the mechanical resonator. In principle, this static shift can act to displace the detuning dependence of the attractor diagram [34,52]; however, for the device considered here this shift is negligible, such that  $\Delta \approx \Delta_0$  (see Appendix B). The physical values of the mechanical amplitude are found to traverse the contours of the attractor diagram that obey the condition  $\Gamma_{\text{tot}} = 0 \Rightarrow \delta\Gamma_m = -\Gamma_m$  [see white dashed line in Fig. 4(e)], corresponding to an increase in mechanical amplitude to dissipate the optical power input to the system [52,53]. As can be seen in Fig. 4(e), for the non-sideband-resolved system considered here, there are two possible mechanical amplitude solutions for optical drive detunings ranging from  $\Delta \approx -2.5$  to  $-4.0 \text{ GHz}$ . This leads to dynamical bistability, and therefore, a hysteresis in the mechanical amplitude, as well as the optomechanical properties of the system [34]. We point out that at the given optical input power, these nonlinear effects, which are photothermal in origin, would not be present for this system if only the radiation-pressure force were considered (see Appendix C).

Fixing the mechanical resonance frequency and damping rate to their low power values of  $\omega_m/2\pi = 11.2 \text{ MHz}$  and  $\Gamma_m/2\pi = 374 \text{ Hz}$ , while using  $\tau = 9.5 \text{ ns}$  determined from finite element method simulations (see Appendix E), we fit the data in Fig. 4 by varying  $G$ ,  $\beta$ ,  $\kappa$ , and  $\kappa_c$ . We note that while driven to self-oscillation, the mechanical frequency locks to a position slightly larger than its off-resonant value [see Fig. 4(c)], which we attribute to a small thermal shift in the mechanical resonance due to optically induced heating of the resonator [42], leading to an additional inconsequential fit parameter. To perform this fitting procedure, we first determine the mechanical amplitude of the resonator as a function of optical drive detuning according to an attractor diagram similar to that in Fig. 4(e) for each iteration of trial

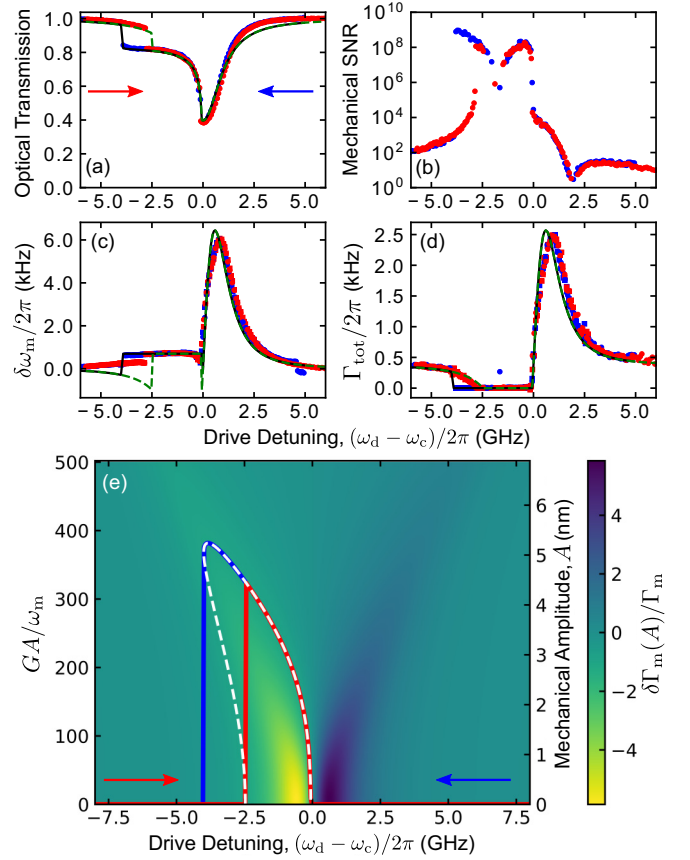


FIG. 4. At an input power of  $P_{\text{in}} = 10.1 \mu\text{W}$ , we find that the photothermal force drives the mechanical resonator into self-oscillation, causing an increase in its amplitude of motion. This results in a highly nonlinear response for (a) the transmission through the optical cavity and (b) the signal-to-noise ratio (SNR) of the homodyne mechanical spectra, as well as the optomechanical (c) spring effect and (d) damping, over the detuning range from  $\Delta \sim 0$  to  $-4 \text{ GHz}$ . In each of these plots, red (blue) data points correspond to an optical drive that was swept starting from the red (blue) side of the optical cavity, i.e., from negative to positive (positive to negative) detunings, as indicated by the arrows in (a) and (e). The data in (c) and (d) are extracted from mechanical spectra obtained using both direct (squares) and homodyne (circles) detection of the high-frequency portion of the optical signal at each drive detuning, while the signal-to-noise ratio in (b) is determined by dividing the maximum value of the homodyne spectra by its off-resonant imprecision noise floor. The data for each detuning takes approximately 5 s to acquire, such that the sweep over the entire  $\sim 160$  detunings occurs on the timescale of  $\sim 800 \text{ s}$ . The dashed green (solid black) lines in (a), (c), and (d) are fits to the red (blue) data using Eqs. (8), (6), and (7), respectively, allowing for extraction of the optomechanical parameters quoted in the main text. In (e), we display the attractor diagram for this system, which is produced by using Eq. (7) to calculate  $\delta\Gamma_m(A)$  for a number of mechanical amplitudes and optical drive detunings. The white dashed line indicates the condition of  $\delta\Gamma_m(A)/\Gamma_m = -1$  (i.e.,  $\Gamma_{\text{tot}} = 0$ ), such that the red (blue) solid line traces out the physical values of the mechanical amplitude for a detuning sweep originating on the red (blue) side of the optical cavity.

parameters. These amplitude are then fed into Eqs. (6), (7), and (8), the results of which are compared to the data in Figs. 4(c), 4(d), and 4(a), respectively. This process is repeated

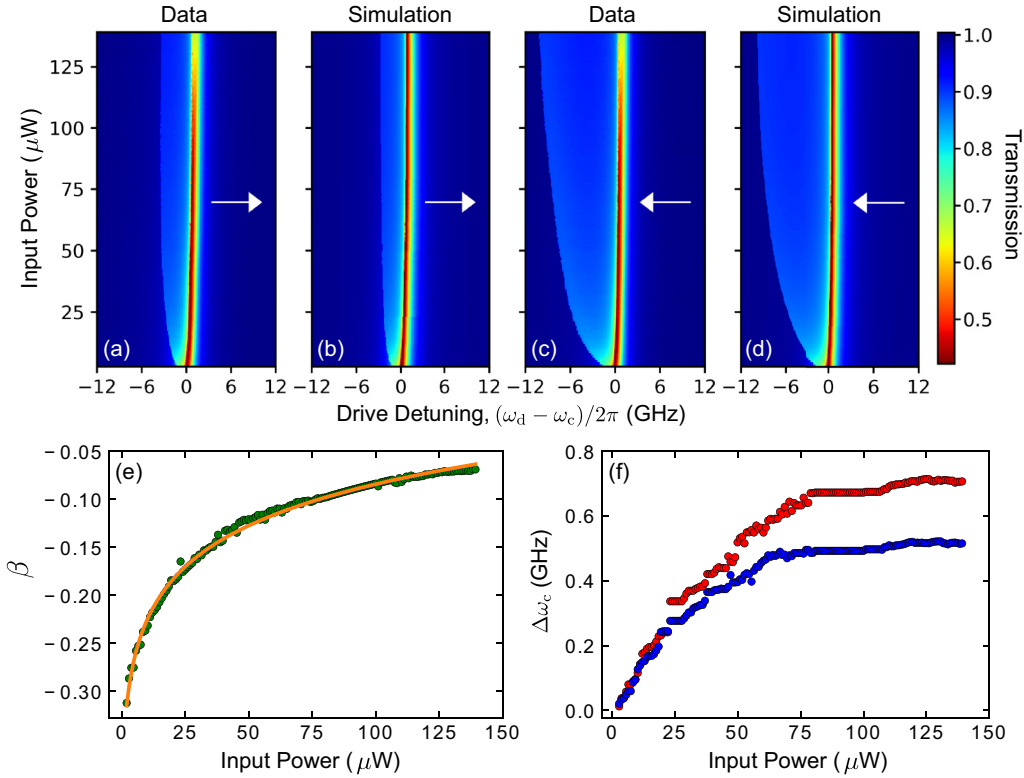


FIG. 5. (a–d) Transmission through the optical cavity as a function of detuning and input power. Here we show (a, c) data and (b, d) simulation for red and blue detuning sweeps (sweep direction indicated by the white arrow), with each detuning scaled to the cavity’s resonance frequency at the lowest measured power of  $P_{\text{in}} = 1.9 \mu\text{W}$ . Fixing  $\kappa/2\pi = 1.59 \text{ GHz}$  and  $\kappa_e/2\pi = 0.29 \text{ GHz}$ , we fit the data in (a, c) to Eq. (8), allowing us to determine  $\beta$  and  $\omega_c$  versus input optical power to the cavity. In (e), we display these values for  $\beta$  (green circles), which are fit to Eq. (11) (orange line) resulting in  $\beta_0 = -0.399$ ,  $B = 0.063$ , and  $P_* = 0.68 \mu\text{W}$ . The simulations in (b, d) are calculated by inputting the values of  $\beta$  from this fit, along with  $\omega_c$  extracted from the fits to (a, c) and the aforementioned fixed values of  $\kappa$  and  $\kappa_e$ , into Eq. (8). Finally, (f) displays the optical cavity resonance frequency shift  $\Delta\omega_c$  (relative to its value at the lowest optical power), with the red/blue data points corresponding to fits of the detuning sweeps originating from the red/blue side of the cavity found in (a, c), both of which indicate a blue shift in the cavity resonance with increasing optical power.

until the minimization condition of the fitting algorithm is met (see Appendix B for more details). Using this procedure, we extract the optomechanical coupling parameters  $G/2\pi = 0.817 \text{ GHz/nm}$  ( $g_0/2\pi = Gx_{\text{zpf}}/2\pi = 52.2 \text{ kHz}$ ) and  $\beta = -0.316$ , as well as a total optical loss rate of  $\kappa/2\pi = 2.04 \text{ GHz}$  and an external coupling rate of  $\kappa_e/2\pi = 0.38 \text{ GHz}$ , for the studied device. This results in a single photon cooperativity of  $\mathcal{C}_0 = 4g_0^2/\kappa\Gamma_m = 1.4 \times 10^{-2}$  and a maximal cavity-enhanced cooperativity of  $\mathcal{C} = \bar{N}_{\text{max}}\mathcal{C}_0 = 68$ , where  $\bar{N}_{\text{max}} = 4\kappa_e P_{\text{in}}/\hbar\omega_c\kappa^2 = 4.7 \times 10^3$  is the average number of photons circulating within the cavity for a resonant pump with an input power of  $P_{\text{in}} = 10.1 \mu\text{W}$ . Furthermore, using these extracted parameters, along with  $\omega_m\tau = 0.67$ , we find  $1 + \omega_m^2\tau^2 = 1.45$  and  $|\beta|\kappa\tau = 38$ . This ensures that Eq. (10) is satisfied, while Eq. (9) is not, confirming that we are indeed in the dueling regime associated with a radiation-pressure-dominated spring effect, but a photothermally driven optomechanical damping.

We continue to observe nonlinear effects in the optical transmission through the cavity for input powers up to  $\sim 140 \mu\text{W}$  (see data in Fig. 5). These measurements are performed under coupling conditions that differ slightly from those used to collect the data in Fig. 4, causing a shift in the loss rates of the optical cavity to  $\kappa/2\pi = 1.59 \text{ GHz}$  and

$\kappa_e/2\pi = 0.29 \text{ GHz}$ . Fixing these values for  $\kappa$  and  $\kappa_e$ , while assuming that the thermal relaxation time remains constant in power/temperature (which should be the case up to roughly 100 K—see Appendix E), we fit the optical scans in Figs. 5(a) and 5(c) to Eq. (8), extracting  $\beta$  and  $\omega_c$  versus optical power input to the cavity [see Figs. 5(e) and 5(f)]. Upon inspection of Fig. 5(e), we find that  $\beta$  exhibits a logarithmic dependence on input power, which can be fit with the phenomenological equation

$$\beta(P) = \beta_0 + B \ln\left(1 + \frac{P}{P_*}\right), \quad (11)$$

where  $\beta_0 = -0.399$  is the value of  $\beta$  at zero input power, while  $B = 0.063$  and  $P_* = 0.68 \mu\text{W}$  are scaling parameters. Rearranging Eq. (11), we can also determine the power at which  $\beta = 0$  as  $P_0 = P_*(e^{-\beta_0/B} - 1) = 384 \mu\text{W}$ . Inputting  $\beta$  from this fit, along with the extracted values of  $\omega_c$  versus power, into Eq. (8), we show that we are able to reproduce the power-dependent behavior of the optical transmission data, as can be seen in Figs. 5(b) and 5(d).

The observed power dependence in  $\beta$  and  $\omega_c$  is likely due to the fact that increasing the power input to the optomechanical cavity causes the system to heat up, changing its thermal and optical properties. Because of the complicated

nature of this optically induced heating, it is difficult to quantitatively ascertain the temperature of the device in this regime; however, we find the qualitative trend that  $\beta$  decreases in magnitude as we move to higher power/temperature. We postulate that this decrease in the magnitude of  $\beta$  with increasing temperature has prevented previous studies of the dueling radiation-pressure and photothermal effects discussed in this paper, as the majority of optomechanical experiments on nanophotonic silicon devices have been performed at room temperature. Furthermore, in Fig. 5(f) it can be seen that  $\omega_c$  increases with power/temperature. This observation is consistent with the negative thermal expansion coefficient of silicon between approximately 17 to 120 K [66], as an increase in temperature reduces the diameter of the microdisk cavity, resulting in a blue-shift of its optical resonant frequency [67,68].

We conclude this section by noting that  $\beta = -0.232$  at  $P_{\text{in}} = 10.2 \mu\text{W}$  for the data in Fig. 5, which is considerably smaller in magnitude than the value of  $\beta = -0.316$  extracted from Fig. 4, where  $P_{\text{in}} = 10.1 \mu\text{W}$ . We attribute this disparity to the discrepancy in optical linewidths between the two measurements, which causes the power absorbed by the mechanical resonator, and therefore its temperature, to be larger for the data in Fig. 5, resulting in a decrease in the magnitude of  $\beta$  (for a more indepth discussion of this effect see Appendix B).

## V. OPTOMECHANICAL COOLING

Up to this point, we have largely focused on the photothermally driven amplification of mechanical motion that occurs for a pump beam detuned to the red side of the optical resonance. However, the photothermal effect can also be used to perform considerable cooling of the mechanical mode on the opposite (blue) side of the resonance [32,33,35,41–43]. For instance, in Fig. 4(d) we find that the photothermal force increases the total damping rate of the mechanical resonator to as high as  $\Gamma_{\text{tot}}/2\pi = 2.5 \text{ kHz}$  at  $\Delta = 2\pi \times 0.97 \text{ GHz}$  ( $= 0.48 \kappa$ ), resulting in a factor of 6.7 increase from its intrinsic value of  $\Gamma_m/2\pi = 374 \text{ Hz}$ . Assuming that the resonator is initially thermalized to the helium bath temperature of  $T_b = 4.2 \text{ K}$ , this damping effect actively cools the mechanical mode to a temperature of  $T_m = T_b(\Gamma_m/\Gamma_{\text{tot}}) = 631 \text{ mK}$ , equivalent to a reduction in the phonon occupation of the mechanical resonator from  $\langle n \rangle \approx 7800$  to  $\langle n \rangle \approx 1170$  [16]. Cooling of this nature is especially intriguing given it occurs for a blue-detuned optical pump, such that the photothermal force must overwhelm any radiation-pressure-driven amplification.

More interesting, however, is the fundamental limit on minimum reachable phonon number using this cooling method, which is set by the shot noise generated by photons impinging upon the mechanical resonator. For a purely radiation-pressure-driven system, this limit is given by

$$\bar{n}_{\text{min}}^{\text{rp}} = -\frac{\frac{\kappa^2}{4} + (\Delta + \omega_m)^2}{4\Delta\omega_m}, \quad (12)$$

which when minimized with respect to detuning in the non-sideband-resolved regime ( $\kappa \gg \omega_m$ ) results in  $\bar{n}_{\text{min}}^{\text{rp}} \approx \kappa/4\omega_m$  [16,69]. It is important to note that this result only holds true for standard, dispersively coupled cavities, as it

has been shown that ground state cooling can in theory be achieved using non-sideband-resolved, dissipatively coupled optomechanical systems [70,71]. Nonetheless, we find that  $\bar{n}_{\text{min}}^{\text{rp}} \approx 45$  for the device studied here, such that it would be impossible to cool it to an average phonon occupation less than one using radiation pressure alone. However, the situation is far more complex when one adds photothermal effects into the picture, as this force interferes with the radiation pressure [26], resulting in a modified expression for the minimum achievable phonon number given by (see Appendix B)

$$\begin{aligned} \bar{n}_{\text{min}} = & -\frac{\frac{\kappa^2}{4} + (\Delta + \omega_m)^2}{4\Delta\omega_m \left\{ \kappa + \frac{\beta}{1+\omega_m^2\tau^2} \left[ \kappa + \tau \left( \frac{\kappa^2}{4} + \Delta^2 - \omega_m^2 \right) \right] \right\}} \\ & \times \left\{ \kappa + \frac{\beta}{1 + \omega_m^2 \tau^2} \left[ \kappa \left( \frac{\beta\kappa}{4\kappa_a} + 1 \right) \right. \right. \\ & \left. \left. + (\Delta - \omega_m) \left( \frac{\beta(\Delta - \omega_m)}{\kappa_a} + 2\omega_m\tau \right) \right] \right\}. \quad (13) \end{aligned}$$

Here we have introduced  $\kappa_a = \eta\kappa_i$  as the optical loss rate due to absorption of photons in the mechanical resonator, which makes up a fraction  $\eta$  of the cavity's total intrinsic loss rate  $\kappa_i$ . For the experimental measurements given in Fig. 4, we determine this total intrinsic loss rate to be  $\kappa_i = \kappa - \kappa_e = 1.66 \text{ GHz}$ . It is difficult to experimentally determine what fraction of this intrinsic loss rate contributes to  $\kappa_a$ ; however, we initially assume that optical losses are dominated by absorption in the mechanical element (i.e., set  $\eta = 1$ ), allowing us to establish a lower limit on the minimum achievable phonon occupation for the device studied here. Using this condition, along with the experimental parameters extracted from the data in Fig. 4, we plot  $\bar{n}_{\text{min}}$  as a function of detuning in Fig. 6(a). As one can see, this minimum achievable phonon number drops below one over a detuning range from  $\Delta \sim \kappa$  to  $9\kappa$ , reaching its optimal value of  $\bar{n}_{\text{min}} = 0.39$  at  $\Delta_{\text{min}} = 3.1\kappa$ , which corresponds to a mechanical resonator that is in its ground state 71% of the time. We note that ground state cooling remains possible when relaxing the condition that  $\kappa_a = \kappa_i$ , with  $\bar{n}_{\text{min}} < 1$  for  $\eta \gtrsim 0.4$  [see inset of Fig. 6(a)]. While it has long been known theoretically that the photothermal force can be used to cool a non-sideband-resolved optomechanical resonator into its motional ground state [25–29], this is the first experimental device reported to exist within the required regime.

To further investigate the parameter space over which ground state photothermal cooling can occur, we have plotted the logarithm of the minimum achievable phonon number versus  $\beta$  and  $\tau$  in Fig. 6(b). Each point on this plot is obtained by varying  $\beta$  and  $\tau$  in Eq. (13) (while again setting all other physical parameters equal to those extracted from the fits in Fig. 4) and taking the minimum value of  $\bar{n}_{\text{min}}$  with respect to detuning. The result is a large region of photothermal parameter space that allows for cooling below the single phonon level, with a slight asymmetry between positive and negative  $\beta$  due to interference between the radiation-pressure and photothermal forces [26]. As indicated by the yellow star in Fig. 6(b), the parameters for the device considered in this work lie well within this regime.

We must be careful, however, when interpreting these results, as  $\bar{n}_{\text{min}}$  describes the fundamental limit on the minimum

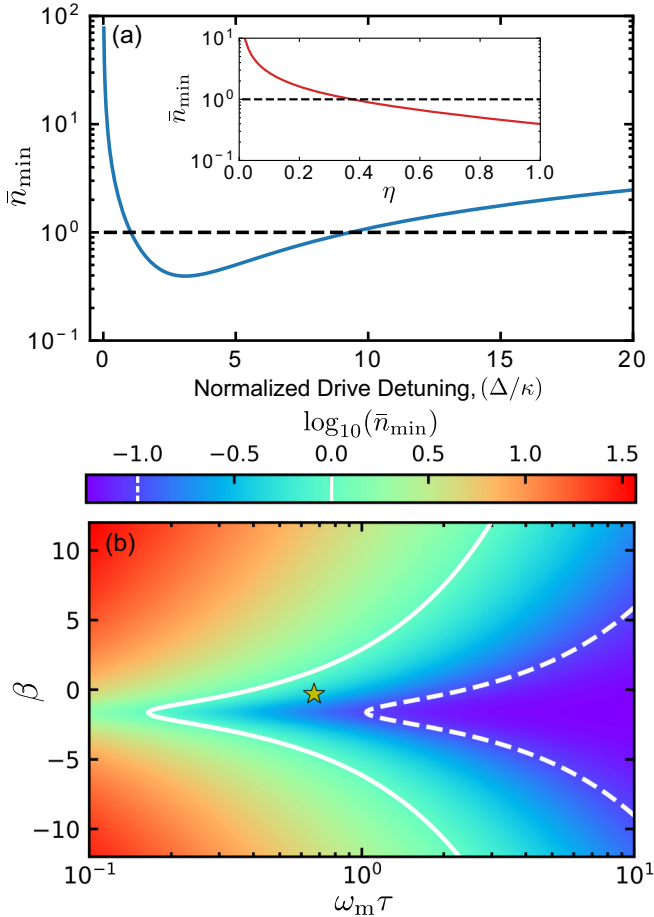


FIG. 6. (a) Plot of the minimum reachable phonon number according to Eq. (13) versus normalized drive detuning using the parameters extracted from the fits in Fig. 4, while setting  $\kappa_a = \kappa_i$ . The black dashed line corresponds to  $\bar{n}_{\min} = 1$ , indicating that the resonator can, in principle, be cooled below single phonon occupancy over a detuning band from  $\Delta \sim \kappa$  to  $9\kappa$ , reaching its minimum value of  $\bar{n}_{\min} = 0.39$  at  $\Delta_{\min} = 3.1\kappa$ . Inset is a plot of this minimum value as a function of the ratio  $\eta = \kappa_a/\kappa_i$ , demonstrating that ground state cooling is still possible for  $\eta \gtrsim 0.4$ . (b) A color plot depicting the base-ten logarithm of  $\bar{n}_{\min}$  (minimized with respect to detuning) as a function of  $\beta$  and  $\tau$ , with the rest of the parameters the same as in (a). Note that while we have expressed the  $x$  axis in terms of the unitless quantity  $\omega_m \tau$ , the mechanical resonance frequency is fixed to  $\omega_m = 2\pi \times 11.2$  MHz such that only  $\tau$  is varied along this axis. Furthermore, we have ensured finite (i.e., nonzero)  $\beta$  to allow us to focus on photothermal effects, as opposed to the narrow feature that emerges due to the radiation-pressure force for very small  $\beta$  ( $\lesssim 0.001$ ). The solid (dashed) white lines demarcate the contour of  $\bar{n}_{\min} = 1$  ( $\bar{n}_{\min} = 0.1$ ), while the yellow star indicates the parameters for the device studied here. As one can see, there is a region where  $\bar{n}_{\min} < 1$  centered near  $\beta = 0$ , with deviations from a symmetric distribution in  $\beta$  being due to interference between the radiation-pressure and photothermal forces [26]. We further note that while  $\bar{n}_{\min}$  decreases for larger values of  $\tau$ , the detuning at which  $\bar{n}_{\min}$  is minimized increases with  $\tau$  (see Appendix B), moving away from  $\Delta \approx \kappa/2$  where the photothermal force is maximal [25], such that it becomes increasingly difficult to reach  $\bar{n}_{\min}$  experimentally.

reachable phonon number using this cooling mechanism. Furthermore, as  $\tau$  increases, so does the detuning at which  $\bar{n}_{\min}$

is minimized, reducing the effectiveness of the photothermal cooling (see Appendix B). Therefore, one generally wishes to maximize the strength of the photothermal damping force, which occurs for  $\omega_m \tau \approx 1$  [25,27,32,33] and  $\Delta \approx \kappa/2$  [see Fig. 4(d)], to decrease the optical power required to reach  $\bar{n}_{\min}$ . Of particular interest are the photothermal cooling parameters of  $\omega_m \tau = 1$  (corresponding to  $\tau = 1/\omega_m = 14.2$  ns) and  $\beta = -2.0$ , which when combined with the other device parameters used in this work, results in  $\bar{n}_{\min} = 0.11$  at  $\Delta_{\min} \approx \kappa/2$  (see Appendix B). These conditions therefore maximize photothermal cooling with respect to both thermal relaxation time and optical drive detuning [25], while still allowing for ground state cooling of the mechanical resonator, thus presenting a set of parameters to strive for in future iterations of the device.

## VI. CONCLUSION

In this paper, we have presented measurements of a silicon whispering-gallery-mode optomechanical cavity that exhibits dynamical backaction effects due to competing photothermal and radiation-pressure forces. We find that the radiation-pressure force governs the optomechanical spring effect, while the photothermal force dictates the optomechanical damping. Furthermore, due to the fact that this photothermal force acts to directly oppose its radiation-pressure counterpart, we find that at high enough power we can reduce the mechanical damping to zero on the red side of the cavity resonance, inducing a parametric instability in the mechanical resonator that drives its motion into large-amplitude self-oscillation. Accompanying this self-oscillating behavior, we observe highly nonlinear effects, as well as a hysteresis depending on the sweep direction of the optical drive, in each of the optomechanical damping, spring effect, and transmission through the optical cavity. Fitting these data with a nonlinear optomechanical model that includes both radiation-pressure and photothermal interactions, we extract the optomechanical properties of the system associated with each of these effects. Finally, using these extracted parameters, we infer that this non-sideband-resolved optomechanical system can theoretically be cooled to an average phonon occupancy less than one. This comprehension of exactly how the radiation-pressure and photothermal forces interact with each other at low temperatures will be crucial as silicon optomechanical cavities continue to be used to perform quantum experiments [6,21,56–58].

While the ability to photothermally cool a non-sideband-resolved optomechanical cavity below single phonon occupancy is promising, reaching this regime in practice presents a significant challenge, largely due to residual heating from inevitable photon absorption processes [26,27]. However, as this device was not purposefully designed for photothermal coupling, it may be possible to engineer this effect to achieve the parameters detailed at the end of the previous section, perhaps by adding a metallic layer to the resonator to enhance its differential thermal contractions and optical absorption [30–37,47]. Furthermore, one could also imagine modifying the thermal time constant by changing the dimensions of the resonator, which would also affect the strength of the photothermal damping. Increasing the photothermal coupling in this way may provide a path to cool a photothermally driven optomechanical device into its motional ground state, as well



as allow for future investigation of other photothermally enhanced optomechanical effects, such as entanglement [28,29] or induced chaos [72,73] between the optical and mechanical modes of the system.

### ACKNOWLEDGMENTS

The authors thank A. Metelmann, A. Clerk, C. Simon, and P. Barclay for valuable discussions. This work was supported by the University of Alberta, Faculty of Science; the Natural Sciences and Engineering Research Council, Canada (Grants No. RGPIN-04523-16, No. DAS-492947-16, and No. CREATE-495446-17); and the Canada Foundation for Innovation. B.D.H. acknowledges support from the Killam Trusts.

### APPENDIX A: EXPERIMENTAL DETAILS

#### 1. Device dimensions

The critical dimensions for the optomechanical device studied in this work (see Fig. 7) are measured using the scanning electron microscope image shown in Fig. 2(a), and are displayed in Table I. These measured device parameters are used when performing finite-element-method simulations of the device.

#### 2. Experimental setup

To address the optomechanical device studied in this work, we use a cryogenic optical detection system (shown schematically in Fig. 8) that allows for both direct detection and homodyne measurements of the collected signal. Light from a fiber-coupled tunable diode laser (1550–1630 nm), whose wavelength is stabilized on long timescales (on the order of hours) using a 2% pickoff to a wavelength meter (WLM), is sent to a variable coupler (VC) that splits the optical circuit into two paths: the signal arm and the local oscillator (LO). The optical power in the signal arm is set using a voltage-controlled variable optical attenuator (VOA), all while being monitored by sending 10% of this signal to a power meter (PM). This path continues through a fiber polarization controller, ensuring that the laser light sent to the optical cavity is polarization-matched to the optical mode of interest. Following these components, the laser in the signal arm is directed via optical fiber to a low temperature optomechanical coupling apparatus that resides on the base plate of a dilution refrigerator [61], complete with a dimpled optical fiber taper [62–64] that allows photons to couple to and from the on-chip optomechanical device. The intracavity signal is recoupled using this tapered fiber and is sent to an optical switch (SW) that toggles this signal

TABLE I. Numerical values for the dimensions of the device studied in this work (see Fig. 7). Measurements were performed using the scanning electron microscope image shown in Fig. 2(a). Device thickness was taken to be  $d = 250$  nm as specified by the manufacturer.

Measured dimensions		
$l_1 = 143$ nm	$w_1 = 177$ nm	$R_d = 595$ nm
$l_2 = 1.53$ $\mu$ m	$w_2 = 177$ nm	$R_c = 5.26$ $\mu$ m
$l_3 = 4.20$ $\mu$ m	$w_3 = 151$ nm	$\theta = 92.7$ deg

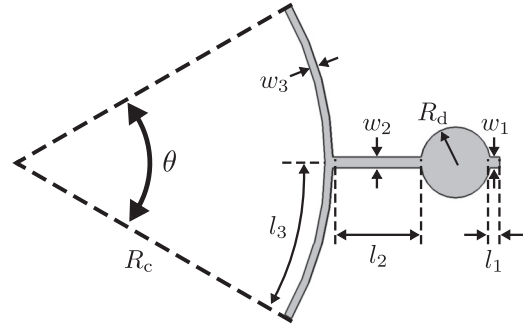


FIG. 7. Schematic of the studied optomechanical device, indicating each of its critical dimensions. Numerical values for each dimension are given in Table I.

between a standard photodetector (PD) for direct detection of the optical signal, or alternatively, to a balanced photodetector (BPD) for homodyne measurements. In the latter case, light from the signal arm is recombined with the LO on a fiber-coupled beam splitter (BS) and sent to the BPD, allowing for a phase-sensitive probe of the optical signal. The constant phase offset between the signal and LO arms is maintained using a proportional-integral-derivative (PID) controlled fiber stretcher (FS) located in the LO, with its setpoint referenced to the low frequency component of the difference signal from the BPD, which is monitored in real-time using a voltmeter (V). For each of the homodyne and direct detection setups, the high frequency signal is recorded as time-series data using a 500 mega-sample per second analog-to-digital converter (ADC), allowing for observation of the mechanical motion. Finally, the transmission through the optical cavity is obtained by monitoring the low frequency ( $< 25$  kHz) channel of the direct detection PD using a data acquisition (DAQ) system.

### APPENDIX B: CAVITY OPTOMECHANICS WITH RADIATION-PRESSURE AND PHOTOTHERMAL INTERACTIONS

In this section, we look to theoretically model the behavior of an optomechanical cavity that is subject to both radiation-pressure and photothermal forces. Specifically, we determine the parameter regimes over which these individual forces dominate each of the optomechanical damping and spring effect, as well as investigate how the inclusion of the photothermal force modifies the optomechanical phenomena of cooling and nonlinear parametric amplification.

To begin, we consider an optical cavity that is dispersively coupled to the displacement of a mechanical resonator in the presence of both radiation-pressure and photothermal forces. Treating the system semiclassically, the equations of motion for the field amplitude  $a$  of the cavity and mechanical position  $x$  of the resonator will be given by [16,25–29,49]

$$\begin{aligned} \dot{a}(t) = & -\frac{\kappa}{2}a(t) + i\Delta_0 a(t) + iGx(t)a(t) + \sqrt{\kappa_e}a_{in}(t) \\ & + \sqrt{\kappa_a}a'_{abs}(t) + \sqrt{\kappa_o}a'_o(t), \end{aligned} \quad (B1)$$

$$\ddot{x}(t) + \Gamma_m \dot{x}(t) + \omega_m^2 x(t) = \frac{1}{m} [F_{th}(t) + F_{rp}(t) + F_{pt}(t)]. \quad (B2)$$

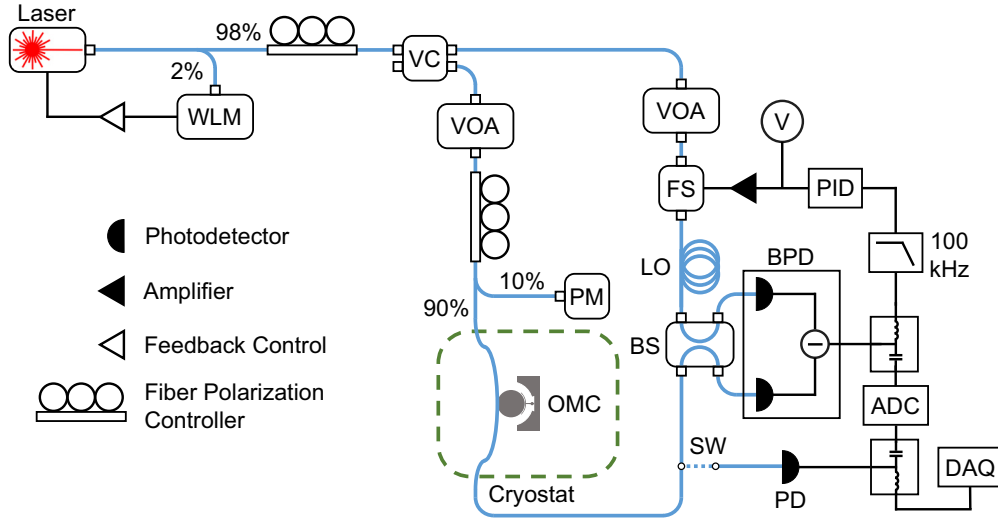


FIG. 8. Schematic of the optical detection system used to probe the optical and mechanical properties of the device under study. WLM = wavelength meter, VC = variable coupler, VOA = variable optical attenuator, PM = power meter, OMC = optomechanical cavity, FS = fiber stretcher, PID = proportional-integral-derivative controller, V = voltmeter, LO = local oscillator, SW = optical switch, BS = beam splitter, BPD = balanced photodetector, PD = photodetector, ADC = analog-to-digital converter, DAQ = data acquisition.

Here,  $\Delta_0 = \omega_d - \omega_c$  is the bare detuning of the optical drive frequency  $\omega_d$  from the resonant frequency of the cavity  $\omega_c$ , while  $\kappa = \kappa_e + \kappa_a + \kappa_o$  is the total decay rate of the optical cavity, composed of contributions from losses to the external coupler, absorption of cavity photons in the mechanical element, and all other sources, at the associated rates of  $\kappa_e$ ,  $\kappa_a$ , and  $\kappa_o$ , respectively. Note that both  $\kappa_a$  and  $\kappa_o$  contribute to the total intrinsic damping rate of the optical cavity  $\kappa_i = \kappa_a + \kappa_o$ . We then have that  $a_{\text{in}}(t)$  is the field input to the cavity via the external coupler, while  $a'_{\text{abs}}(t)$  and  $a'_o(t)$  are the field operators associated with vacuum noise (denoted by primes) that creeps into the system via absorption of photons in the mechanical element and other loss channels, with each of these input operators having units of  $1/\sqrt{s}$ . Meanwhile,  $\omega_m$ ,  $\Gamma_m$ , and  $m$  are the resonant frequency, damping rate, and effective mass of the mechanical resonator, which is actuated by an intrinsic thermal fluctuation force  $F_{\text{th}}$ , as well as two optically driven forces, the radiation-pressure force [16,49]

$$F_{\text{rp}}(t) = \hbar G a^\dagger(t) a(t) \quad (\text{B3})$$

and the photothermal force [25–29,49]

$$F_{\text{pt}}(t) = \frac{\hbar G \beta}{\kappa_a \tau} \int_{-\infty}^t e^{-\frac{t-t'}{\tau}} a_{\text{abs}}^\dagger(t') a_{\text{abs}}(t') dt'. \quad (\text{B4})$$

Here,  $G = -d\omega_c/dx$  is the dispersive optomechanical coupling coefficient and  $a_{\text{abs}}(t) = \sqrt{\kappa_a} a(t) - a'_{\text{abs}}(t)$  is the field operator characterizing the photons absorbed by the mechanical resonator [25,26,28]. The mathematical form of this photothermal force is motivated by the fact that adiabatic elimination of the mechanical resonator's phononic bath [43] gives rise to an integral of an exponential that decays on a time scale set by the photothermal time constant  $\tau$  (see Appendix E for more details). Also included in Eq. (B4) is the dimensionless parameter  $\beta$  that determines the relative strength and direction of the photothermal force with respect to the radiation-pressure force. It is important to note that it is

possible for  $\beta$  to be negative in value [32–35,39,41,42], such that the photothermal force acts to directly oppose radiation-pressure effects. Finally, while we have chosen to identify the force in Eq. (B4) as photothermal in nature, with the appropriate choice of  $\tau$ ,  $\beta$ , and  $\kappa_a$ , the description that follows can be applied to any optical force that is delayed in time.

### 1. Linearized optomechanical equations of motion

To solve the equations of motion for the above optomechanical system, we express each quantity as a combination of its classical, steady-state amplitude (denoted by an overhead bar) and its fluctuations about this mean value (denoted by an operator hat). This leads to  $a(t) = \bar{a} + \hat{a}(t)$ ,  $a_{\text{in}}(t) = \bar{a}_{\text{in}} + \hat{a}'_{\text{in}}(t)$ ,  $a'_{\text{abs}}(t) = \bar{a}'_{\text{abs}}(t) + \hat{a}'_{\text{abs}}(t)$ ,  $a'_o(t) = \bar{a}'_o(t) + \hat{a}'_o(t)$ ,  $x(t) = \bar{x} + \hat{x}(t)$ , and  $F_{\text{th}}(t) = \bar{F}_{\text{th}}(t) + \hat{F}_{\text{th}}(t)$ . Note that each of the noise quantities [i.e.,  $\hat{a}'_{\text{abs}}(t)$ ,  $\hat{a}'_o(t)$ , and  $\hat{F}_{\text{th}}(t)$ ] are composed solely of a fluctuating term (which includes both thermal and quantum noise). In putting each of these relations into Eqs. (B1)–(B4), while only keeping terms to first order in the fluctuations, we linearize Eqs. (B1) and (B2), resulting in

$$\begin{aligned} \hat{a}(t) = & -\frac{\kappa}{2} \hat{a}(t) + i\Delta \hat{a}(t) + iG \bar{a} \hat{x}(t) + \sqrt{\kappa_e} \hat{a}'_{\text{in}}(t) \\ & + \sqrt{\kappa_a} \hat{a}'_{\text{abs}}(t) + \sqrt{\kappa_o} \hat{a}'_o(t), \end{aligned} \quad (\text{B5})$$

$$\begin{aligned} & \ddot{\hat{x}}(t) + \Gamma_m \dot{\hat{x}}(t) + \omega_m^2 \hat{x}(t) \\ = & \frac{1}{m} \left( \hat{F}_{\text{th}}(t) + \hbar G [\bar{a}^* \hat{a}(t) + \bar{a} \hat{a}^\dagger(t)] \right. \\ & + \frac{\hbar G \beta}{\tau} \int_{-\infty}^t e^{-\frac{t-t'}{\tau}} \left\{ [\bar{a}^* \hat{a}(t') + \bar{a} \hat{a}^\dagger(t')] \right. \\ & \left. \left. - \frac{1}{\sqrt{\kappa_a}} [\bar{a}^* \hat{a}'_{\text{abs}}(t') + \bar{a} \hat{a}'_{\text{abs}}^\dagger(t')] \right\} dt \right), \end{aligned} \quad (\text{B6})$$

with the steady-state values of  $a$  and  $x$  being

$$\bar{a} = \frac{\sqrt{\kappa_e \bar{a}_{\text{in}}}}{\kappa/2 - i\Delta}, \quad (\text{B7})$$

$$\bar{x} = \frac{\hbar G |\bar{a}|^2 (1 + \beta)}{m\omega_m^2}. \quad (\text{B8})$$

Note that we have also introduced a modified drive detuning  $\Delta = \Delta_0 + G\bar{x}$  to account for the static shift in cavity frequency due to the steady-state displacement of the mechanical equilibrium position.

In this linearized form, Eqs. (B5) and (B6) can now be Fourier transformed, resulting in the frequency representation of the cavity field and mechanical displacement fluctuations as

$$\hat{a}(\omega) = \chi_c(\omega) [iG\bar{x}\hat{x}(\omega) + \sqrt{\kappa_e}\hat{a}'_{\text{in}}(\omega) + \sqrt{\kappa_a}\hat{a}'_{\text{abs}}(\omega) + \sqrt{\kappa_o}\hat{a}'_o(\omega)], \quad (\text{B9})$$

$$\hat{x}(\omega) = \chi_m(\omega) \left( \hat{F}_{\text{th}}(\omega) + \hbar G \left\{ \left( 1 + \frac{\beta}{1 - i\omega\tau} \right) [\bar{a}^* \hat{a}(\omega) + \bar{a} \hat{a}^\dagger(\omega)] - \frac{\beta}{\sqrt{\kappa_a}(1 - i\omega\tau)} [\bar{a}^* \hat{a}'_{\text{abs}}(\omega) + \bar{a} \hat{a}'_{\text{abs}}{}^\dagger(\omega)] \right\} \right). \quad (\text{B10})$$

Here we have implicitly used the fact that for a given variable  $\hat{\delta}$ , we have  $\hat{\delta}^\dagger(\omega) = [\hat{\delta}(-\omega)]^\dagger$  (note that  $[\hat{x}(-\omega)]^\dagger = \hat{x}(\omega)$  as position is a Hermitian quantity) [16], as well as introduced the frequency-dependent susceptibilities of the optical cavity  $\chi_c(\omega)$  and mechanical resonator  $\chi_m(\omega)$  as

$$\chi_c(\omega) = \frac{1}{\kappa/2 - i(\Delta + \omega)}, \quad (\text{B11})$$

$$\chi_m(\omega) = \frac{1}{m(\omega_m^2 - \omega^2 - i\omega\Gamma_m)}. \quad (\text{B12})$$

In what follows, we will use the linearized, frequency-dependent solutions for  $\hat{a}$  and  $\hat{x}$  given in Eqs. (B9) and (B10) to investigate a number of optomechanical effects.

## 2. Optomechanical damping and spring effect

To determine the optomechanical damping and spring effect, we input Eq. (B9) into Eq. (B10), resulting in

$$\hat{x}(\omega) = \chi_{\text{eff}}(\omega) \left( \hat{F}_{\text{th}}(\omega) + \hbar G \left\{ \left( 1 + \frac{\beta}{1 - i\omega\tau} \right) \times (\chi_c(\omega)\bar{a}^*[\sqrt{\kappa_e}\hat{a}'_{\text{in}}(\omega) + \sqrt{\kappa_a}\hat{a}'_{\text{abs}}(\omega) + \sqrt{\kappa_o}\hat{a}'_o(\omega)] + \chi_c^*(-\omega)\bar{a}[\sqrt{\kappa_e}\hat{a}'_{\text{in}}{}^\dagger(\omega) + \sqrt{\kappa_a}\hat{a}'_{\text{abs}}{}^\dagger(\omega) + \sqrt{\kappa_o}\hat{a}'_o{}^\dagger(\omega)]) - \frac{\beta}{\sqrt{\kappa_a}(1 - i\omega\tau)} [\bar{a}^* \hat{a}'_{\text{abs}}(\omega) + \bar{a} \hat{a}'_{\text{abs}}{}^\dagger(\omega)] \right\} \right), \quad (\text{B13})$$

where we have introduced the effective mechanical susceptibility as [16,25,26,28,49]

$$\begin{aligned} \chi_{\text{eff}}^{-1}(\omega) &= \chi_m^{-1}(\omega) \\ &\quad - i\hbar G^2 |\bar{a}|^2 \left( 1 + \frac{\beta}{1 - i\omega\tau} \right) [\chi_c(\omega) - \chi_c^*(-\omega)] \\ &\equiv m[(\omega_m + \delta\omega_m)^2 - \omega^2 - i\omega(\Gamma_m + \delta\Gamma_m)] \\ &\approx m[\omega_m^2 - \omega^2 + 2\omega_m\delta\omega_m - i\omega\Gamma_m - i\omega\delta\Gamma_m]. \end{aligned} \quad (\text{B14})$$

Note that we have assumed  $\delta\omega_m \ll \omega_m$  for the approximation made in the last line of Eq. (B14). From this effective susceptibility, we can extract the optomechanically induced shift in the mechanical resonance frequency, or optomechanical spring effect,

$$\begin{aligned} \delta\omega_m &= -\frac{\hbar G^2 |\bar{a}|^2}{2m\omega_m} \text{Re} \left\{ i \left( 1 + \frac{\beta}{1 - i\omega_m\tau} \right) \right. \\ &\quad \times [\chi_c(\omega_m) - \chi_c^*(-\omega_m)] \left. \right\} \\ &= 2\bar{N}g_0^2\Delta |\chi_c(\omega_m)|^2 |\chi_c(-\omega_m)|^2 \\ &\quad \times \left[ \frac{\kappa^2}{4} + \Delta^2 - \omega_m^2 \right. \\ &\quad \left. + \frac{\beta}{1 + \omega_m^2\tau^2} \left( \frac{\kappa^2}{4} + \Delta^2 - \omega_m^2 - \omega_m^2\kappa\tau \right) \right], \end{aligned} \quad (\text{B15})$$

as well as the shift in the mechanical damping rate, or optomechanical damping,

$$\begin{aligned} \delta\Gamma_m &= \frac{\hbar G^2 |\bar{a}|^2}{m\omega_m} \text{Im} \left\{ i \left( 1 + \frac{\beta}{1 - i\omega_m\tau} \right) \right. \\ &\quad \times [\chi_c(\omega_m) - \chi_c^*(-\omega_m)] \left. \right\} \\ &= -4\bar{N}g_0^2\Delta\omega_m |\chi_c(\omega_m)|^2 |\chi_c(-\omega_m)|^2 \\ &\quad \times \left\{ \kappa + \frac{\beta}{1 + \omega_m^2\tau^2} \left[ \kappa + \tau \left( \frac{\kappa^2}{4} + \Delta^2 - \omega_m^2 \right) \right] \right\}. \end{aligned} \quad (\text{B16})$$

Here  $\bar{N} = |\bar{a}|^2$  is the average number of coherent photons (originating from the drive field) that are confined to the optical cavity, while  $g_0 = Gx_{\text{zpf}}$  is the single-photon, single-phonon optomechanical coupling rate, with  $x_{\text{zpf}} = \sqrt{\hbar/2m\omega_m}$  being the zero-point fluctuation amplitude of the mechanical resonator. Note that we have also taken  $\omega \approx \omega_m$  in Eqs. (B15) and (B16), as we are only concerned with effects near mechanical resonance. As expected, these dynamical backaction effects vanish for zero detuning ( $\Delta = 0$ ) and the standard radiation-pressure-driven expressions are restored when  $\beta = 0$  [16].

We are now interested in determining the parameter space for which the optomechanical damping and spring effect are dominated by photothermal forces. By inspection of Eqs. (B15) and (B16), we find that this will occur for the

spring effect when

$$\left| \frac{\kappa^2}{4} + \Delta^2 - \omega_m^2 \right| < \left| \frac{\beta}{1 + \omega_m^2 \tau^2} \left( \frac{\kappa^2}{4} + \Delta^2 - \omega_m^2 - \omega_m^2 \kappa \tau \right) \right|, \quad (\text{B17})$$

while the photothermal force will dominate the optomechanical damping if

$$\kappa < \left| \frac{\beta}{1 + \omega_m^2 \tau^2} \left[ \kappa + \tau \left( \frac{\kappa^2}{4} + \Delta^2 - \omega_m^2 \right) \right] \right|. \quad (\text{B18})$$

These inequalities are simplified considerably if we restrict ourselves to the experimentally relevant parameter space of  $\kappa \gg \omega_m$  (i.e., the non-sideband-resolved regime) and  $\omega_m \tau \sim 1$ , which together imply  $\kappa \tau \gg 1$ . Using these conditions, Eq. (B17) will be satisfied if

$$1 + \omega_m^2 \tau^2 \lesssim |\beta|, \quad (\text{B19})$$

while Eq. (B18) becomes

$$\kappa < \frac{|\beta| \tau}{1 + \omega_m^2 \tau^2} \left( \frac{\kappa^2}{4} + \Delta^2 \right). \quad (\text{B20})$$

Finally, Eq. (B20) can be further simplified if we assume  $\Delta \sim \pm \kappa/2$ , i.e., only consider the region where optomechanical damping is maximized, which results in

$$1 + \omega_m^2 \tau^2 \lesssim \frac{|\beta| \kappa \tau}{2}. \quad (\text{B21})$$

Note that for the above inequalities we have taken the absolute value of  $\beta$  as it can be positive or negative depending on the orientation of the photothermal force with respect to the radiation-pressure force. From Eqs. (B19)–(B21) it is therefore clear that for  $\kappa \tau \gg 1$  (as is assumed here and is experimentally relevant for this work), it is possible to have values of  $\beta$  and  $\tau$  such that radiation-pressure forces dominate the spring effect, while photothermal effects dictate the optomechanical damping. We note that this is especially important in the non-sideband-resolved regime, where  $\kappa$  is generally large, as highlighted by the fact that photothermal damping effects are often stronger in non-sideband-resolved cavities when compared to their sideband-resolved counterparts [25,26,28,29]. Furthermore, if  $\beta < 0$ , the photothermal and radiation-pressure forces oppose each other, resulting in an oddly similar detuning dependence between the optomechanical spring effect and damping [see Figs. 1(c) and 1(f)] in apparent violation of the Kramers-Kronig relations [17].

### 3. Optomechanical cooling

We now look to see how the inclusion of a photothermal force acts to modify conventional radiation-pressure-driven backaction cooling. To do this, we begin by determining the two-sided spectral density of the mechanical displacement  $S_{xx}(\omega)$  in the presence of optomechanical effects, which can be found by using [74]

$$S_{xx}(\omega) = \frac{1}{2\pi} \int_{-\infty}^{\infty} \langle \hat{x}(\omega) \hat{x}(\omega') \rangle d\omega', \quad (\text{B22})$$

along with the following Markovian noise correlators [16,25]

$$\langle \hat{F}_{\text{th}}(\omega) \hat{F}_{\text{th}}(\omega') \rangle = 2\pi \hbar \omega m \Gamma_m \coth\left(\frac{\hbar \omega}{2k_B T}\right) \delta(\omega + \omega'), \quad (\text{B23})$$

$$\langle \hat{a}'_i(\omega) \hat{a}'_i(\omega') \rangle = 2\pi \delta(\omega + \omega'), \quad (\text{B24})$$

$$\langle \hat{a}'_i(\omega) \hat{a}'_i(\omega') \rangle = \langle \hat{a}'_i(\omega) \hat{a}'_i(\omega') \rangle = \langle \hat{a}'_i(\omega) \hat{a}'_i(\omega') \rangle = 0. \quad (\text{B25})$$

In Eqs. (B24) and (B25) we have used  $\hat{a}'_i$  as a placeholder for any of the optical vacuum fluctuation amplitudes  $\hat{a}'_{\text{in}}$ ,  $\hat{a}'_{\text{abs}}$ , and  $\hat{a}'_{\text{o}}$ , as well as assumed a zero temperature bath for each optical mode (due to the fact that  $\hbar \omega_c \gg k_B T$ ). We further note that any cross-correlations between the noise terms given in Eqs. (B23)–(B25) will equate to zero. Inputting Eqs. (B13) and (B23)–(B25) into Eq. (B22), while using the fact that  $\chi_{\text{eff}}(-\omega) = \chi_{\text{eff}}^*(\omega)$  [this is a direct consequence of  $\chi_{\text{eff}}(t)$  being a real-valued function], we then find

$$S_{xx}(\omega) = |\chi_{\text{eff}}(\omega)|^2 [S_{FF}^{\text{th}}(\omega) + S_{FF}^{\text{opt}}(\omega)], \quad (\text{B26})$$

where

$$\begin{aligned} S_{FF}^{\text{th}}(\omega) &= \frac{1}{2\pi} \int_{-\infty}^{\infty} \langle \hat{F}_{\text{th}}(\omega) \hat{F}_{\text{th}}(\omega') \rangle d\omega' \\ &= \hbar \omega m \Gamma_m \coth\left(\frac{\hbar \omega}{2k_B T}\right) \end{aligned} \quad (\text{B27})$$

is the spectral density of the thermal force [25,74–76] and  $S_{FF}^{\text{opt}}(\omega) = S_{FF}^{\text{rp}}(\omega) + S_{FF}^{\text{pt}}(\omega)$  is the optical force spectral density, composed of the spectra due to radiation-pressure  $S_{FF}^{\text{rp}}(\omega)$  and photothermal  $S_{FF}^{\text{pt}}(\omega)$  effects. We further find it convenient to express these optical force spectra as  $S_{FF}^{\text{rp}}(\omega) = \hbar^2 G^2 S_{NN}^{\text{rp}}(\omega)$  and  $S_{FF}^{\text{pt}}(\omega) = \hbar^2 G^2 S_{NN}^{\text{pt}}(\omega)$ , where

$$S_{NN}^{\text{rp}}(\omega) = \frac{\bar{N} \kappa}{(\Delta + \omega)^2 + (\kappa/2)^2} \quad (\text{B28})$$

and

$$\begin{aligned} S_{NN}^{\text{pt}}(\omega) &= \frac{\bar{N}}{(\Delta + \omega)^2 + (\kappa/2)^2} \frac{\beta}{1 + \omega^2 \tau^2} \\ &\times \left\{ \kappa \left( \frac{\beta \kappa}{4\kappa_a} + 1 \right) + (\Delta + \omega) \left[ \frac{\beta(\Delta + \omega)}{\kappa_a} - 2\omega\tau \right] \right\} \end{aligned} \quad (\text{B29})$$

are the effective cavity photon number spectra associated with the radiation-pressure and photothermal forces, respectively [69,75].

Using the spectral density function given by Eq. (B26), we can determine the mean-squared value of the mechanical displacement as [74]

$$\langle x^2 \rangle = \frac{1}{2\pi} \int_{-\infty}^{\infty} S_{xx}(\omega) d\omega. \quad (\text{B30})$$

To perform this integral, we make the approximation

$$|\chi_{\text{eff}}(\omega)|^2 \approx \frac{\pi}{2m^2 \omega_m^2 \Gamma_{\text{tot}}} [\delta(\omega - \omega_m) + \delta(\omega + \omega_m)], \quad (\text{B31})$$

where  $\Gamma_{\text{tot}} = \Gamma_m + \delta\Gamma_m$  is the total mechanical damping rate, including both the intrinsic mechanical damping and

optomechanical effects. This approximation is valid for high- $Q$  mechanical resonators (i.e.,  $Q_m = \omega_m/\Gamma_m \gg 1$ ), due to the fact that the majority of the mechanical displacement spectrum is located near  $\omega \approx \pm\omega_m$ . Using this approximation to evaluate the integral in Eq. (B30), we find

$$\langle x^2 \rangle = \frac{x_{\text{zpf}}^2}{\Gamma_{\text{tot}}} \left\{ (2\bar{n}_{\text{th}} + 1)\Gamma_m + g_0^2 [S_{NN}^{\text{opt}}(\omega_m) + S_{NN}^{\text{opt}}(-\omega_m)] \right\}, \quad (\text{B32})$$

where we have taken advantage of the relation  $\coth(\hbar\omega_m/2k_B T) = 2\bar{n}_{\text{th}} + 1$ , with  $\bar{n}_{\text{th}} = (e^{\hbar\omega_m/k_B T} - 1)^{-1}$  being the average thermal phonon occupation number of the bath (according to Bose-Einstein statistics) evaluated at the mechanical resonance frequency. Comparing Eq. (B32) to the expected expression for the mean-squared displacement,  $\langle x^2 \rangle = 2x_{\text{zpf}}^2 \langle n \rangle + \frac{1}{2}$  [74], we determine the average phonon occupancy  $\langle n \rangle$  of the mechanical resonator to be

$$\langle n \rangle = \frac{(2\bar{n}_{\text{th}} + 1)\Gamma_m + g_0^2 [S_{NN}^{\text{opt}}(\omega_m) + S_{NN}^{\text{opt}}(-\omega_m)]}{2\Gamma_{\text{tot}}} - \frac{1}{2}. \quad (\text{B33})$$

Finally, using the identity [26,69,75]

$$\begin{aligned} \delta\Gamma_m &= \frac{x_{\text{zpf}}^2}{\hbar^2} [S_{FF}^{\text{opt}}(\omega_m) - S_{FF}^{\text{opt}}(-\omega_m)] \\ &= g_0^2 [S_{NN}^{\text{opt}}(\omega_m) - S_{NN}^{\text{opt}}(-\omega_m)], \end{aligned} \quad (\text{B34})$$

we can recast Eq. (B33) into the familiar rate equation form [16,27,69]

$$\langle n \rangle = \frac{\bar{n}_{\text{th}}\Gamma_m + \bar{n}_{\text{min}}\delta\Gamma_m}{\Gamma_{\text{tot}}}, \quad (\text{B35})$$

allowing us to identify the minimum attainable average phonon occupancy using this cooling method as [16,26,69]

$$\begin{aligned} \bar{n}_{\text{min}} &= [S_{FF}^{\text{opt}}(\omega_m)/S_{FF}^{\text{opt}}(-\omega_m) - 1]^{-1} \\ &= [S_{NN}^{\text{opt}}(\omega_m)/S_{NN}^{\text{opt}}(-\omega_m) - 1]^{-1} \\ &= -\frac{\frac{\kappa^2}{4} + (\Delta + \omega_m)^2}{4\Delta\omega_m \left\{ \kappa + \frac{\beta}{1 + \omega_m^2 \tau^2} \left[ \kappa + \tau \left( \frac{\kappa^2}{4} + \Delta^2 - \omega_m^2 \right) \right] \right\}} \\ &\quad \times \left( \kappa + \frac{\beta}{1 + \omega_m^2 \tau^2} \left\{ \kappa \left( \frac{\beta\kappa}{4\kappa_a} + 1 \right) \right. \right. \\ &\quad \left. \left. + (\Delta - \omega_m) \left[ \frac{\beta(\Delta - \omega_m)}{\kappa_a} + 2\omega_m\tau \right] \right\} \right). \end{aligned} \quad (\text{B36})$$

As expected, by setting  $\beta = 0$ , Eq. (B36) reverts to the standard radiation pressure result [16,69]

$$\bar{n}_{\text{min}}^{\text{rp}} = -\frac{\frac{\kappa^2}{4} + (\Delta + \omega_m)^2}{4\Delta\omega_m}. \quad (\text{B37})$$

Furthermore, if we sever the connection to the optomechanical bath [i.e., set  $G = g_0 = 0$  such that  $\delta\Gamma_m = 0$  in Eqs. (B33) and (B35)], the mechanical resonator thermalizes to its environmental bath such that  $\langle n \rangle = \bar{n}_{\text{th}}$ .

The quantity in Eq. (B36) describes the minimum attainable phonon occupation of the mechanical resonator (when considering both radiation-pressure and photothermal forces), which can be reached if  $\delta\Gamma_m$  is large enough such that

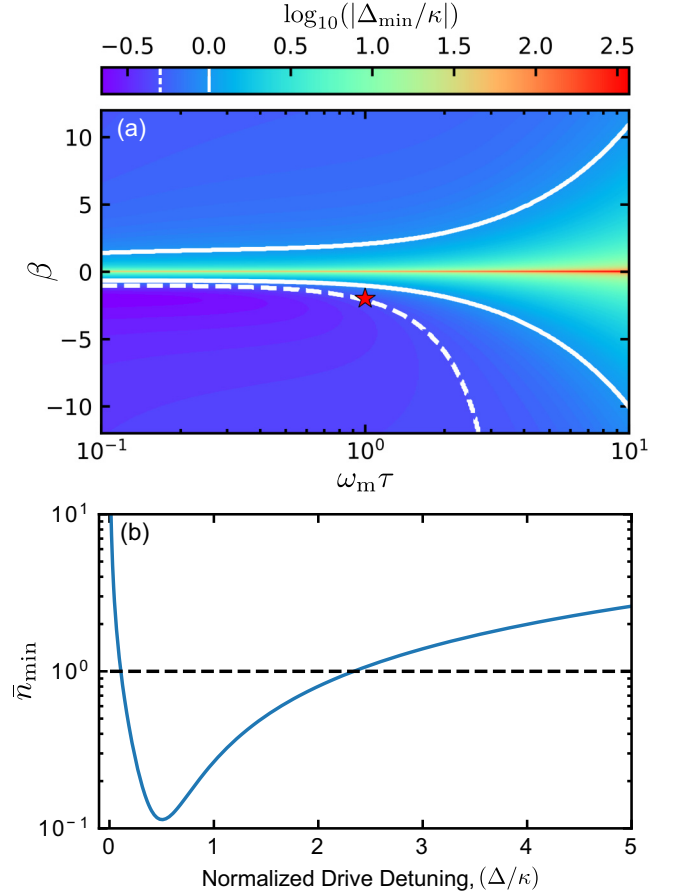


FIG. 9. (a) Color plot of  $\log_{10}(|\Delta_{\text{min}}/\kappa|)$ , i.e., the base-ten logarithm of the absolute value of the detuning  $\Delta_{\text{min}}$  for which  $\bar{n}_{\text{min}}$  is globally minimized (normalized by  $\kappa$ ). Here we have used the same optomechanical parameters as those in Fig. 6, with the solid (dashed) white line indicating the contour of  $|\Delta_{\text{min}}| = \kappa$  ( $|\Delta_{\text{min}}| = \kappa/2$ ). Note that the sign of  $\Delta_{\text{min}}$  is opposite of  $\beta$ , such that  $\Delta_{\text{min}} < 0$  ( $\Delta_{\text{min}} > 0$ ) for  $\beta > 0$  ( $\beta < 0$ ). As one can see,  $|\Delta_{\text{min}}|$  is maximized near  $\beta = 0$  and increases for larger values of  $\tau$ . We point out, however, that for small  $\beta$  and large  $\tau$ , local minima emerge near  $\Delta \approx -\kappa/2$  [not shown here as (a) depicts the global minimum of  $\bar{n}_{\text{min}}$ ], corresponding to the region over which radiation-pressure effects begin to dominate. Furthermore, as is seen with  $\bar{n}_{\text{min}}$  in Fig. 6(b),  $|\Delta_{\text{min}}|$  is asymmetric about  $\beta = 0$ , which is again due to interference between radiation-pressure and photothermal effects. Finally, we note that the dashed contour of  $\Delta_{\text{min}} = \kappa/2$  passes very near  $\beta = -2.0$  for  $\omega_m\tau = 1$  (see red star), such that these parameters optimize photothermal cooling versus both optical drive detuning and thermal relaxation time [25]. In (b), we plot  $\bar{n}_{\text{min}}$  versus normalized drive detuning for this special set of parameters, showing that the lowest achievable phonon number is indeed minimized to  $\bar{n}_{\text{min}} = 0.11$  at  $\Delta_{\text{min}} \approx \kappa/2$ .

$\Gamma_{\text{tot}} \approx \delta\Gamma_m$  and  $\bar{n}_{\text{th}}\Gamma_m \ll \bar{n}_{\text{min}}\delta\Gamma_m$ . In this sense, Eqs. (B33) and (B35) do not include effects that would arise when experimentally performing optomechanical cooling of the mechanical resonator, such as the inevitable heating due to photon absorption [26,27]. Nevertheless, the inclusion of photothermal effects has a substantial influence on this minimal phonon occupation when compared to the result obtained using solely radiation pressure. In fact, due to interference between the radiation-pressure and photothermal forces [26], it is possible to cool the mechanical resonator to an average

phonon occupancy below one while operating in the non-sideband-resolved regime [25–29], a feat which is not possible for a dispersively coupled, radiation-pressure-driven optomechanical cavity [16,69].

To determine the absolute minimum phonon occupancy that can be reached for a given optomechanical cavity, the expressions in Eqs. (B36) and (B37) must be optimized with respect to the optical drive detuning  $\Delta$ . This is easily done for the case of radiation pressure alone, where Eq. (B37) is found to be minimized for  $\Delta_{\min}^{\text{rp}} = -\sqrt{\kappa^2/4 + \omega_m^2}$ . Therefore, in the non-sideband-resolved regime,  $\Delta_{\min}^{\text{rp}} \approx -\kappa/2$ , leading to  $\bar{n}_{\min}^{\text{rp}} \approx \kappa/4\omega_m$  [16]. Unfortunately, the situation is far more complicated when the photothermal force is included, such that we are unable to determine a closed-form solution for the detuning  $\Delta_{\min}$  that minimizes Eq. (B36). However,  $\Delta_{\min}$  can be determined numerically for a given set of conditions, as we have shown in Fig. 9(a) for the same parameter space that is mapped out in Fig. 6(b). Here we see that  $|\Delta_{\min}|$  grows for decreasing  $\beta$  and increasing  $\tau$ , moving away from the optimal value of  $|\Delta_{\min}| \approx \kappa/2$  denoted by the white dashed line, while exhibiting a similar asymmetry about  $\beta$  as was seen for  $\bar{n}_{\min}$ . Interestingly, this plot further shows that near  $\beta = -2.0$  and  $\omega_m\tau = 1$ , we find  $\Delta_{\min} \approx \kappa/2$  [see red star in Fig. 9(a)], such that for this set of parameters the strength of the photothermal force is maximized with respect to both detuning and thermal relaxation time [25,27,32,33], while still allowing for ground state cooling of the mechanical motion to an occupancy as low as  $\bar{n}_{\min} = 0.11$  [see Fig. 9(b)].

#### 4. Nonlinear optomechanics

In the previous sections of this Appendix, we implicitly assumed an optomechanical system whose mechanical fluctuations are small enough to allow for a linearized treatment of the equations of motion. However, when the amplitude of oscillation  $A$  of the mechanical resonator becomes large enough ( $GA \gg \omega_m$ ), the system enters into a regime where keeping terms to first order in their fluctuations no longer suffices. One such situation where this occurs is optomechanical self-amplification [34,52–55,77–79], which onsets when  $\delta\Gamma_m = -\Gamma_m$ , such that  $\Gamma_{\text{tot}}$  drops to zero and a parametric instability emerges, driving the mechanical motion into large amplitude oscillations to counteract the optical drive forces.

Here we will study this nonlinear optomechanical interaction in the same context as the previous sections, where we include both radiation-pressure and photothermal effects. However, as the large amplitude mechanical oscillations associated with this nonlinear regime act to overwhelm any quantum noise [i.e., terms containing  $a'_{\text{in}}(t)$ ,  $a'_{\text{abs}}(t)$ , or  $a'_o(t)$ ], we restrict ourselves to a classical treatment of the optomechanical system, such that Eqs. (B1) and (B2) become

$$\dot{a}(t) = -\frac{\kappa}{2}a(t) + i\Delta_0 a(t) + iGx(t)a(t) + \sqrt{\kappa_e}\bar{a}_{\text{in}}, \quad (\text{B38})$$

$$\ddot{x}(t) + \Gamma_m\dot{x}(t) + \omega_m^2 x(t) = \frac{1}{m}[F_{\text{th}}(t) + F_{\text{rp}}(t) + F_{\text{pt}}(t)]. \quad (\text{B39})$$

Furthermore, we introduce the classical radiation-pressure force  $F_{\text{rp}}(t) = \hbar G|a(t)|^2$ , along with the classical photother-

mal force by modifying Eq. (B4) to obtain

$$F_{\text{pt}}(t) = \frac{\hbar G\beta}{\tau} \int_{-\infty}^t e^{-\frac{t-t'}{\tau}} |a(t')|^2 dt'. \quad (\text{B40})$$

We continue by assuming a high- $Q$  mechanical system, such that we can use the ansatz [16,52,53]

$$x(t) = \bar{x} + A \cos(\omega_m t), \quad (\text{B41})$$

as the solution to Eq. (B39) for the resonator's displacement, where again  $\bar{x}$  is the resonator's static displacement from equilibrium. Inputting this expression into Eq. (B38), we solve for the optical field amplitude as

$$a(t) = \sqrt{\kappa_e}\bar{a}_{\text{in}} e^{i\phi(t)} \sum_{k=-\infty}^{\infty} \alpha_k e^{ik\omega_m t}, \quad (\text{B42})$$

with  $\phi(t) = \xi \sin(\omega_m t)$  being the time-dependent global phase of the field and

$$\alpha_k = \frac{J_k(-\xi)}{\kappa/2 - i(\Delta_0 + G\bar{x} - k\omega_m)}, \quad (\text{B43})$$

where  $J_k(z)$  is the  $k$ th Bessel function of the first kind and  $\xi = GA/\omega_m$  is the dimensionless mechanical modulation strength [16,52–54,59]. We point out that in the expression for  $\alpha_k$ , we have explicitly written out the optical drive detuning  $\Delta = \Delta_0 + G\bar{x}$ , as we wish to be more transparent with the  $\bar{x}$  term throughout this section for completeness. Note, however, that for the experiment considered in this work, the effect of adding this  $G\bar{x}$  term to the bare drive detuning is negligible, such that  $\Delta \approx \Delta_0$ . This is demonstrated by the fact that even at the largest optical power input to the device ( $P_{\text{in}} = 139 \mu\text{W}$ ), we find the maximum static displacement of the resonator to be  $\bar{x}_{\text{max}} = 46 \text{ pm}$ , causing a shift in the detuning that is at most  $G\bar{x}_{\text{max}} = 38 \text{ MHz} = 0.024\kappa$ .

We now look to determine the quantities  $\bar{x}$ ,  $\delta\omega_m$ , and  $\delta\Gamma_m$  in terms of the mechanical amplitude  $A$  using this nonlinear optomechanical treatment. In doing so, we neglect the thermal force acting upon the resonator, as its effect will be dwarfed by that of its optically induced counterparts. Starting by taking the time average of Eq. (B39) (i.e., balancing the time-averaged forces of the system), we find [16,34,52,53]

$$\bar{x}(A) = \frac{\hbar G\kappa_e |\bar{a}_{\text{in}}|^2}{m\omega_m^2} (1 + \beta) \sum_{k=-\infty}^{\infty} |\alpha_k|^2, \quad (\text{B44})$$

where we have used the fact that  $\langle \ddot{x}(t) \rangle = \langle \dot{x}(t) \rangle = 0$  and  $\langle x(t) \rangle = \bar{x}$ , as well as

$$\langle |a(t)|^2 \rangle = \kappa_e |\bar{a}_{\text{in}}|^2 \sum_{k=-\infty}^{\infty} |\alpha_k|^2, \quad (\text{B45})$$

$$\left\langle \frac{\beta}{\tau} \int_{-\infty}^t e^{-\frac{t-t'}{\tau}} |a(t')|^2 dt' \right\rangle = \beta \kappa_e |\bar{a}_{\text{in}}|^2 \sum_{k=-\infty}^{\infty} |\alpha_k|^2. \quad (\text{B46})$$

Note that since  $\alpha_k$  is implicitly dependent on  $\bar{x}$ , Eq. (B44) represents a transcendental equation for  $\bar{x}$  in terms of  $A$  and  $\Delta_0$  (see Fig. 10), which in general must be solved numerically.

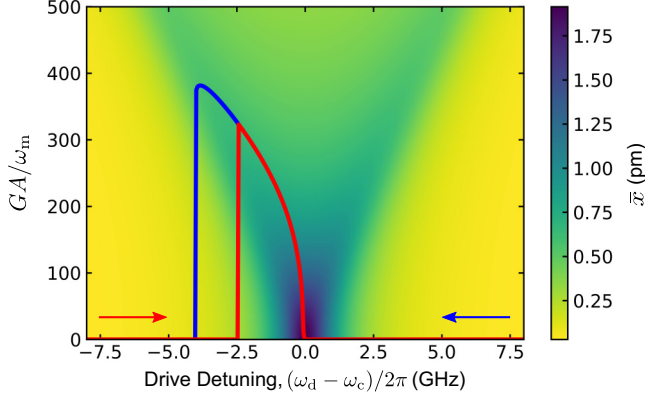


FIG. 10. A color plot of  $\bar{x}$  versus mechanical amplitude and optical drive detuning for the conditions given in Fig. 4. The solid lines are the mechanical amplitudes that are traced out for detuning sweeps performed in the direction of the corresponding colored arrows (see Fig. 4). Thus, these contours denote the physical values of  $\bar{x}$  that are realized in this situation.

Next, we multiply Eq. (B39) by  $\dot{x}(t)$  and again take the time average, balancing the time-averaged power of the system. This leads to the condition that  $\Gamma_{\text{tot}} = \Gamma_m + \delta\Gamma_m(A) = 0$  [16,34,52,53], such that we can identify the amplitude-dependent optomechanical damping of the system as

$$\delta\Gamma_m(A) = \frac{2\hbar G\kappa_e |\bar{a}_{\text{in}}|^2}{A m \omega_m} \sum_{k=-\infty}^{\infty} \text{Im} \left[ \alpha_k \alpha_{k+1}^* \left( 1 + \frac{\beta}{1 - i\omega_m \tau} \right) \right]. \quad (\text{B47})$$

Note that to obtain this result, we have used the relations  $\langle \ddot{x}(t)\dot{x}(t) \rangle = \langle x(t)\dot{x}(t) \rangle = 0$  and  $\langle \dot{x}^2(t) \rangle = \omega_m^2 A^2/2$ , along with

$$\langle |a(t)|^2 \dot{x}(t) \rangle = -A \omega_m \kappa_e |\bar{a}_{\text{in}}|^2 \sum_{k=-\infty}^{\infty} \text{Im} \{ \alpha_k \alpha_{k+1}^* \}, \quad (\text{B48})$$

$$\left\langle \frac{\beta}{\tau} \int_{-\infty}^t e^{-t'/\tau} |a(t')|^2 \dot{x}(t) dt' \right\rangle = -A \omega_m \kappa_e |\bar{a}_{\text{in}}|^2 \sum_{k=-\infty}^{\infty} \text{Im} \left\{ \frac{\beta \alpha_k \alpha_{k+1}^*}{1 - i\omega_m \tau} \right\}. \quad (\text{B49})$$

Finally, it can also be shown (see Ref. [80], for example) that the spring effect in the nonlinear optomechanical regime will be given by

$$\delta\omega_m(A) = -\frac{\hbar G\kappa_e |\bar{a}_{\text{in}}|^2}{A m \omega_m} \times \sum_{k=-\infty}^{\infty} \text{Re} \left[ \alpha_k \alpha_{k+1}^* \left( 1 + \frac{\beta}{1 - i\omega_m \tau} \right) \right]. \quad (\text{B50})$$

Interestingly, one can use the time-averaged energy balance equation [by multiplying Eq. (B39) by  $x(t)$  and time-averaging], along with the relations  $\langle \dot{x}(t)x(t) \rangle = 0$ ,  $\langle \ddot{x}(t)x(t) \rangle = -\omega_m^2 A^2/2$ , and  $\langle x^2(t) \rangle = \bar{x}^2 + A^2/2$ , to show that  $\delta\omega_m(A) = 0$  while  $A$  is large enough that the system

remains in the nonlinear regime. This frequency locking effect, coupled with the reduction of the resonance linewidth, is indicative of phonon lasing in the mechanical resonator [16].

We are also interested in how mechanical self-oscillations affect the transmission of the optical field through the cavity. To do this, we consider the optical field output from the cavity, which can be found using input-output theory as  $a_{\text{out}}(t) = a_{\text{in}}(t) - \sqrt{\kappa_e} a(t)$  [16]. Inserting Eq. (B42) into this expression, while only considering the time-independent terms, we find the amplitude-dependent transmission through the cavity as [16,59]

$$\mathcal{T}(A) = \frac{|\bar{a}_{\text{out}}|^2}{|\bar{a}_{\text{in}}|^2} = 1 - 2\kappa_e \text{Re} \left\{ \sum_{k=-\infty}^{\infty} J_{-k}(\xi) \alpha_k \right\} + \kappa_e^2 \sum_{k=-\infty}^{\infty} |\alpha_k|^2, \quad (\text{B51})$$

where we have used the Jacobi-Anger expansion [50]

$$e^{\pm i\phi(t)} = \sum_{k=-\infty}^{\infty} J_{-k}(\xi) e^{\pm ik\omega_m t}. \quad (\text{B52})$$

We conclude this section by noting that in the regime of small mechanical oscillations (i.e.,  $\xi \ll 1$ ), each of the amplitude-dependent quantities given above approach their linearized counterpart. That is, Eq. (B44)  $\rightarrow$  Eq. (B8), Eq. (B47)  $\rightarrow$  Eq. (B16), and Eq. (B50)  $\rightarrow$  Eq. (B15), while Eq. (B51) approaches its linearized version given by [16]

$$\mathcal{T}_{\text{lin}} = 1 - \kappa_e (\kappa - \kappa_e) |\chi_c(0)|^2 = 1 - \frac{\kappa_e \kappa_i}{\Delta^2 + (\kappa/2)^2}. \quad (\text{B53})$$

## 5. Integral approximations

Though the expressions in the previous section provide exact representations for the optomechanical shift in mechanical equilibrium position, damping, and spring effect, computing these quantities numerically can be cumbersome. This is due to the fact that to accurately model the nonlinear behavior of the optomechanical system, the number of terms that one must keep for each of the sums found in Eqs. (B44)–(B51) is on the order of  $\xi$ , which can be as large as 1500 for the conditions studied here. Fortunately, it was shown by Metzger *et al.* [34] that in the non-sideband-resolved regime, the integral in Eq. (B40) can be performed directly by assuming the optical intensity inside the cavity adiabatically follows the quasistatic motion of the mechanical resonator. This allows for a simpler, more computationally efficient treatment of the nonlinear optomechanical system considered in this work, with minimal error introduced into the final results when compared to those given by Eqs. (B44), (B47), and (B50) (see Fig. 11 for instance). Here we provide a brief overview of this method, resulting in approximate expressions for each of the nonlinear optomechanical properties given in the previous section.

For this integral approach, we immediately assume the non-sideband-resolved regime, such that the optical field in the cavity reacts nearly instantaneously to the resonator's mechanical motion [34]. This allows us to treat  $x(t)$  as a quasistatic variable, such that we can insert the ansatz given

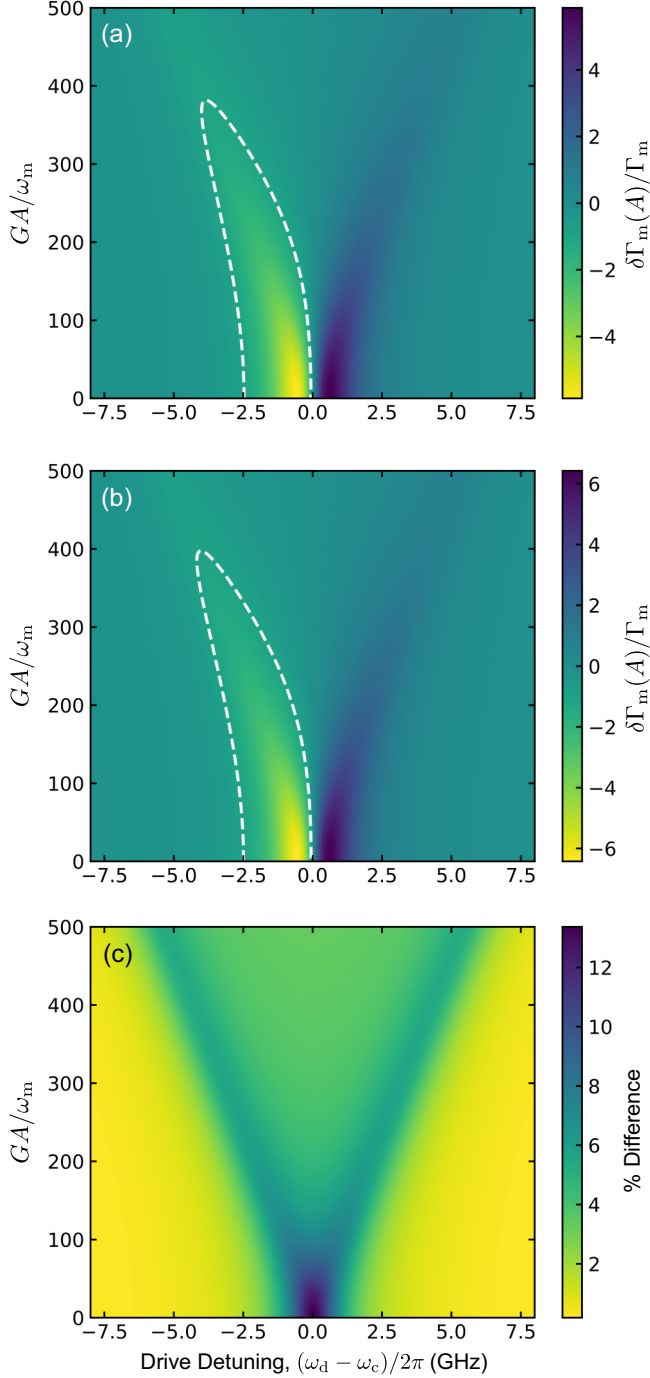


FIG. 11. Attractor diagrams of  $\delta\Gamma_m(A)/\Gamma_m$  (color scale) for the device parameters given in Fig. 4 using (a) the exact sum formalism of Eqs. (B44) and (B47), and (b) the integral approximations given by Eqs. (B55) and (B59). The white dashed line indicates the contour of  $\delta\Gamma_m(A)/\Gamma_m = -1$ , demarcating the region of self-oscillations. For the sums in (a), terms up to  $k = \pm 1000$  were used, while the integrals in (b) were performed using a numerical solver (trapezoidal method). In (c), we show the percent difference between the attractor diagrams given in (a) and (b). Here, we highlight the fact that over the displayed detuning and amplitude range, there is at most a 13.4% difference between the sum and integral methods for calculating  $\delta\Gamma_m(A)$ , with this maximum discrepancy located near zero detuning for small mechanical amplitudes.

by Eq. (B41) into Eq. (B7) [i.e., by taking  $\Delta = \Delta_0 + G\bar{x} + GA \cos(\omega_m t)$ ] to directly solve for the quasistatic cavity field amplitude as

$$a(t) = \frac{\sqrt{\kappa_e} \bar{a}_{\text{in}}}{\kappa/2 - i[\Delta_0 + G\bar{x} + GA \cos(\omega_m t)]}. \quad (\text{B54})$$

Using this approximate expression, we can again take the time average of Eq. (B39) to find an integral form for  $\bar{x}$  as

$$\bar{x}(A) = \frac{\hbar G \kappa_e |\bar{a}_{\text{in}}|^2 (1 + \beta)}{2\pi m \omega_m^2} \times \int_0^{2\pi} \frac{d\phi}{(\kappa/2)^2 + (\Delta_0 + G\bar{x} + GA \cos \phi)^2}. \quad (\text{B55})$$

In comparing this expression to what was found for  $\bar{x}$  in Appendix B4, we see that this approximation is equivalent to replacing the sum in Eq. (B44) with an integral according to

$$\sum_{k=-\infty}^{\infty} |\alpha_k|^2 \approx \frac{1}{2\pi} \int_0^{2\pi} \frac{d\phi}{(\kappa/2)^2 + (\Delta_0 + G\bar{x} + GA \cos \phi)^2}. \quad (\text{B56})$$

Furthermore, this integral can be solved analytically, resulting in

$$\int_0^{2\pi} \frac{d\phi}{(\kappa/2)^2 + (\Delta_0 + G\bar{x} + GA \cos \phi)^2} = \frac{2\pi\sqrt{2}}{\kappa\sqrt{A}} \sqrt{\sqrt{A} + B}, \quad (\text{B57})$$

where  $A = B^2 + \kappa^2(\Delta_0 + G\bar{x})^2$  and  $B = G^2 A^2 + \kappa^2/4 - (\Delta_0 + G\bar{x})^2$ . Therefore, we can write  $\bar{x}$  in the purely analytical form

$$\bar{x}(A) = \frac{\sqrt{2}\hbar G \kappa_e |\bar{a}_{\text{in}}|^2 (1 + \beta)}{m \omega_m^2 \kappa} \frac{\sqrt{\sqrt{A} + B}}{\sqrt{A}}. \quad (\text{B58})$$

Performing a similar analysis to determine the integral form for  $\delta\Gamma_m(A)$ , we multiply Eq. (B39) by  $\dot{x}(t)$  and take the time average, while using the approximation for  $a(t)$  given by Eq. (B54) to obtain

$$\delta\Gamma_m(A) = \frac{\hbar G \kappa_e |\bar{a}_{\text{in}}|^2 \beta}{\pi A m \omega_m} \frac{\omega_m \tau}{1 + \omega_m^2 \tau^2} \times \int_0^{2\pi} \frac{\cos \phi d\phi}{(\kappa/2)^2 + (\Delta_0 + G\bar{x} + GA \cos \phi)^2}. \quad (\text{B59})$$

We note that this integral expression is only valid in the regime where photothermal forces dominate the optomechanical damping [see Eq. (B18)], as  $\delta\Gamma_m(A) = 0$  for  $\beta = 0$  here. Similar to the integral expression for  $\bar{x}$ , we find that Eq. (B59) approximates Eq. (B47) by replacing its sum with the integral

$$\sum_{k=-\infty}^{\infty} \text{Im} \left\{ \alpha_k \alpha_{k+1}^* \left( 1 + \frac{\beta}{1 - i\omega_m \tau} \right) \right\} \approx \frac{\beta}{2\pi} \frac{\omega_m \tau}{1 + \omega_m^2 \tau^2} \int_0^{2\pi} \frac{\cos \phi d\phi}{(\kappa/2)^2 + (\Delta_0 + G\bar{x} + GA \cos \phi)^2}. \quad (\text{B60})$$



This integral also has an analytical expression given by

$$\begin{aligned} & \int_0^{2\pi} \frac{\cos \phi d\phi}{(\kappa/2)^2 + (\Delta_0 + G\bar{x} + GA \cos \phi)^2} \\ &= -\text{sgn}(\Delta_0 + G\bar{x}) \frac{2\pi\sqrt{2}}{GA\kappa\sqrt{\mathcal{A}}} \left( |\Delta_0 + G\bar{x}| \sqrt{\sqrt{\mathcal{A}} - \mathcal{B}} \right. \\ & \quad \left. - \frac{\kappa}{2} \sqrt{\sqrt{\mathcal{A}} - \mathcal{B}} \right), \end{aligned} \quad (\text{B61})$$

where  $\text{sgn}(z)$  is the signum function. Using this relation, we can then express  $\delta\Gamma_m$  in the analytical form

$$\begin{aligned} \delta\Gamma_m(A) &= \frac{-2\sqrt{2}\hbar\kappa_e|\bar{a}_{\text{in}}|^2\beta}{A^2m\omega_m\kappa} \frac{\omega_m\tau}{1+\omega_m^2\tau^2} \frac{\text{sgn}(\Delta_0 + G\bar{x})}{\sqrt{\mathcal{A}}} \\ & \quad \times \left( |\Delta_0 + G\bar{x}| \sqrt{\sqrt{\mathcal{A}} - \mathcal{B}} - \frac{\kappa}{2} \sqrt{\sqrt{\mathcal{A}} - \mathcal{B}} \right). \end{aligned} \quad (\text{B62})$$

It is also possible to arrive at an integral expression for  $\delta\omega_m$ , which looks similar to Eq. (B59) except the factor of  $\cos(\phi)$  in the numerator of the integrand is replaced by  $\sin(\phi)$ . This, however, results in an integral that evaluates to zero, as one would expect in the self-oscillating regime (see Appendix B 4), and therefore offers no additional insight into Eq. (B50).

In Fig. 11, we compare the attractor diagrams of  $\delta\Gamma_m(A)$  for the optomechanical device studied in this work generated using both the exact sums given in Eqs. (B44) and (B47), as well as the integral approximations of Eqs. (B55) and (B59). As our device exists deeply within the non-sideband-resolved regime ( $\kappa/\omega_m \approx 180$ ) and has a large photothermal contribution to the optomechanical damping ( $|\beta|\kappa\tau = 38$ ), the integral approximations presented in this section accurately model its nonlinear optomechanical behavior. This is demonstrated by the fact the percent difference in  $\delta\Gamma_m(A)$  between these two methods is at most 13.4% for the conditions given in Fig. 4 [see Fig. 11(c)]. Furthermore, we note that while the integral approach slightly overshoots the value of  $\delta\Gamma_m(A)$ , it still provides an excellent approximation of the mechanical amplitude, as can be seen by the nearly matching contour lines in Figs. 11(a) and 11(b).

We conclude this section by noting that while we have used Eqs. (B55)–(B62) for preliminary assessment of our optomechanical device, as well as the computationally intensive calculations associated with the varying power measurements shown in Fig. 5, the fits and attractor diagram in Fig. 4 were determined using the exact expressions given by Eqs. (B44)–(B51).

## 6. Optical power transfer

In this section, we use the input-output formalism introduced in Appendix B 4, along with the conservation of energy, to investigate the power input to and output from the optical cavity, as well as absorbed by the mechanical resonator and dissipated via other loss mechanisms (see Fig. 12). Restricting ourselves to a linearized classical treatment (all quantum effects will average to zero), we begin with the power input to the optical cavity, which can be expressed in terms of its

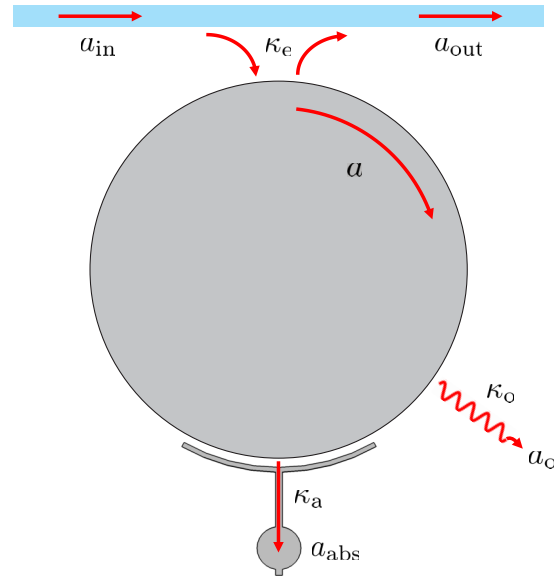


FIG. 12. Schematic illustrating the flow of the optical field through the optomechanical cavity.

field amplitude as  $P_{\text{in}} = \hbar\omega_d|\bar{a}_{\text{in}}|^2$  [16]. The power recollectd by the external waveguide (and subsequently sent to our detection apparatus) is then simply given by (see Appendix B 4)

$$P_{\text{out}} = \hbar\omega_d|\bar{a}_{\text{out}}|^2 = P_{\text{in}} \left[ 1 - \frac{\kappa_e\kappa_i}{\Delta^2 + (\kappa/2)^2} \right]. \quad (\text{B63})$$

Meanwhile, the power absorbed by the mechanical resonator is determined to be

$$P_{\text{abs}} = \hbar\omega_d|\bar{a}_{\text{abs}}|^2 = P_{\text{in}} \frac{\kappa_e\kappa_a}{\Delta^2 + (\kappa/2)^2}. \quad (\text{B64})$$

Finally, power lost to other cavity dissipation channels is found as

$$P_o = \hbar\omega_d|\bar{a}_o|^2 = P_{\text{in}} \frac{\kappa_e\kappa_o}{\Delta^2 + (\kappa/2)^2}, \quad (\text{B65})$$

where  $\bar{a}_o = \sqrt{\kappa_o}\bar{a}$  is the steady-state field amplitude associated with these damping mechanisms. We note that Eqs. (B63)–(B65) obey the conservation of energy in the sense that  $P_{\text{in}} = P_{\text{out}} + P_{\text{abs}} + P_o$ .

Equation (B64) has very important consequences for optically induced heating of the mechanical resonator. This is due to the fact that even if the same amount power is input to the cavity, differing values of  $\kappa_e$  and  $\kappa_i$ , and therefore  $\kappa$ , can cause varying amounts of power to be absorbed by the resonator, causing it to heat to different temperatures. For instance, inputting the values of  $\kappa$  and  $\kappa_e$  from the two different coupling conditions used to obtain the data found in Figs. 4 and 5 (while assuming  $\kappa_a$  remains the same in each case), we find the power absorbed by the mechanical resonator (on cavity resonance) to be approximately 25% larger for the data in Fig. 5 compared to that in Fig. 4. This effect, coupled with the rapid decrease in  $\beta$  at low optical input powers

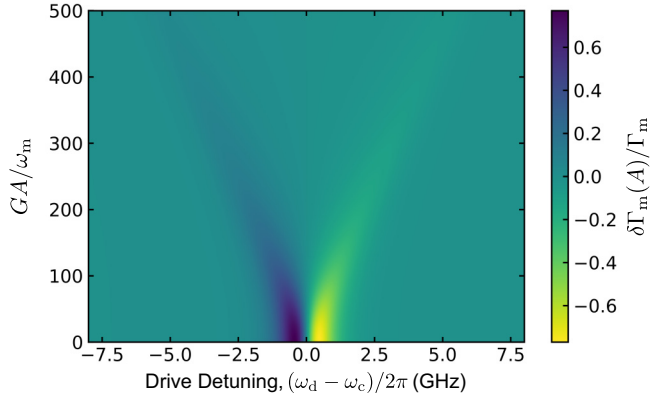


FIG. 13. Attractor diagram of  $\delta\Gamma_m(A)/\Gamma_m$  for the device parameters given in Fig. 4, except with  $\beta = 0$  such that only radiation-pressure effects are present. We note that not only does the sign of the optomechanical damping reverse, restoring what one would expect for a radiation-pressure-driven system, but the damping force is no longer strong enough to induce mechanical self-oscillations at this power ( $P_{\text{in}} = 10.1 \mu\text{W}$ ), as demonstrated by the fact that  $\delta\Gamma_m(A)/\Gamma_m > -1$  for all optical drive detunings.

[see Fig. 5(e)], likely accounts for the reason why  $\beta$  differs between these two data sets for similar input powers.

### APPENDIX C: RADIATION-PRESSURE-DRIVEN ATTRACTOR

To understand how substantial photothermal effects are in determining the optomechanical properties of the studied device, it is interesting to investigate the attractor diagram with only the radiation-pressure force present. To do this, we have produced an attractor diagram for the device parameters given in Fig. 4 while setting  $\beta = 0$  such that the photothermal force is negated. The result is drastic (see Fig. 13), as the absence of photothermal effects causes the detuning dependence of the optomechanical damping to reverse. Furthermore, we show that with the radiation-pressure force alone, this system is no longer able to be driven into self-oscillations at the considered optical input power of  $P_{\text{in}} = 10.1 \mu\text{W}$ . It is therefore clear that the addition of the photothermal force has significant effects on the optomechanical properties of the system.

### APPENDIX D: POWER DEPENDENCE OF OPTOMECHANICAL PROPERTIES

#### 1. Spring effect and damping

Along with the studies shown in Figs. 3–5, we have also investigated the optomechanical properties of our device over nearly three orders of magnitude in input optical power from approximately 50 nW to  $10 \mu\text{W}$ , as seen in Fig. 14. Most importantly, we observe that for all input powers, the optomechanical damping exhibits the same qualitative behavior as the optical spring effect, similar to what is seen in Figs. 3(d) and 3(f), as well as Figs. 4(c) and 4(d). Such a power dependence is in agreement with an optomechanical damping caused by dueling radiation-pressure and photothermal forces, as both of these effects scale identically with optical input power [see Eqs. (B16) and (B47)].

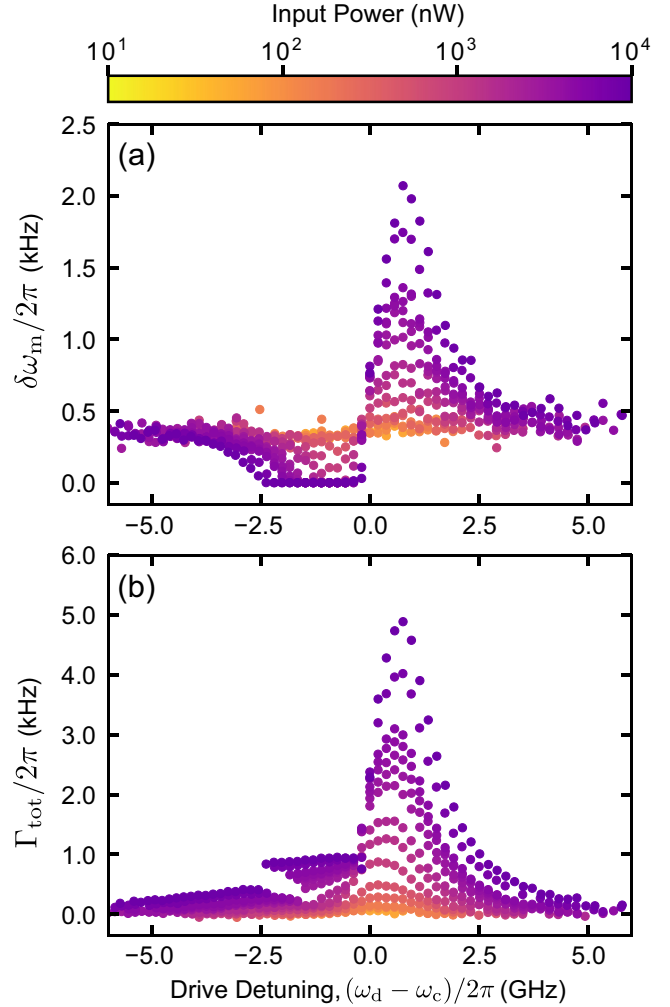


FIG. 14. Optomechanical (a) spring effect and (b) damping over nearly three orders of magnitude in input optical power, ranging from approximately 50 nW to  $10 \mu\text{W}$ . Even at very low powers, optomechanical damping occurs for a blue-detuned optical drive, qualitatively matching the detuning dependence of the optomechanical spring effect.

#### 2. Hysteresis in optical transmission

Due to the bistable nature of the attractor diagram shown in Fig. 4(e), amplification of the mechanical resonator’s motion results in hysteretic behavior of the transmission through the cavity depending on whether the pump beam swept from its red or blue side. As the optical power input to the cavity is increased, optomechanical amplification occurs over a larger range of drive detunings, causing this hysteresis spacing to expand. In Fig. 15, we showcase this effect for the data in Figs. 5(a) and 5(c), where we demonstrate that at high input powers ( $P_{\text{in}} \gtrsim 25 \mu\text{W}$ ), the hysteresis spacing roughly obeys a square-root dependence.

### APPENDIX E: PHOTOTHERMAL RELAXATION TIME

The photothermal time constant  $\tau$  that was introduced in Eq. (3) is a very important quantity that sets the time scale, and in some instances the strength, of photothermally driven

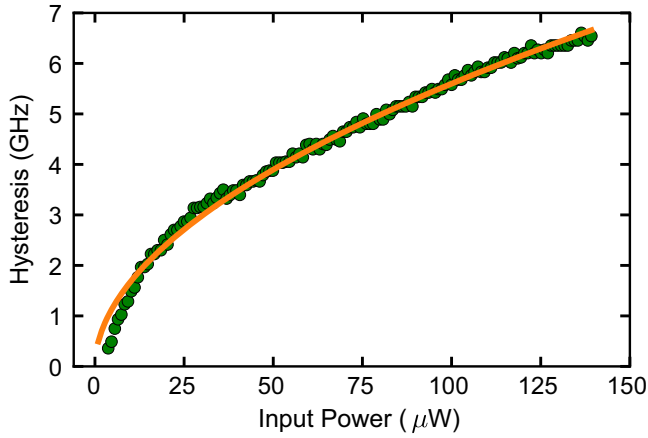


FIG. 15. Hysteresis spacing of the transmission through the cavity versus optical input power (green circles) extracted from the data in Figs. 5(a) and 5(c). The orange line is a fit to a power law, from which we find an exponent of 0.52, indicating a near square-root dependence of the hysteresis spacing on input optical power.

optomechanical effects. For a thin beam of rectangular cross section, Zener showed that this time constant is dominated by thermal relaxation of the fundamental mode of the beam, resulting in

$$\tau = \frac{l^2 C_p}{\pi^2 k_{\text{th}}}, \quad (\text{E1})$$

where  $l$ ,  $C_p$ , and  $k_{\text{th}}$  are the length, volumetric heat capacity at constant pressure (with units of  $\text{J}/\text{m}^3 \text{K}$ ), and thermal conductivity of the beam, respectively [81–83]. For a nonmagnetic, crystalline insulator (e.g., silicon), the thermal properties of the material are governed by its phonons, such that at low temperatures its heat capacity can be determined according to the Debye model as [84]

$$C_p = \frac{2\pi^2 k_B^4 T^3}{5\hbar^3 c_s^3}, \quad (\text{E2})$$

where  $c_s = (\frac{1}{3} \sum_i \frac{1}{c_i^3})^{-1/3}$  is the effective speed of sound in the material, with the sum taken over the single longitudinal ( $l$ ) and two transverse ( $t_1$ ,  $t_2$ ) phonon polarizations. For silicon, this effective speed is given by  $c_s = 5718$  m/s, where we have taken  $c_l = 9148$  m/s,  $c_{t_1} = 4679$  m/s, and  $c_{t_2} = 5857$  m/s [64]. Furthermore, treating the phonons as a diffuse, noninteracting gas, we can express the thermal conductivity as [84]

$$k_{\text{th}} = \frac{1}{3} C_p \Lambda c_s = \frac{2\pi^2 k_B^4 T^3 \Lambda}{15\hbar^3 c_s^2}, \quad (\text{E3})$$

where  $\Lambda$  is the phonon mean free path, which is in general temperature-dependent [85]. However, as pointed out by Casimir [86], below a certain temperature this mean free path will become comparable to the dimensions of the system, such that it will be limited by the device's finite size. We note that for the resonator studied in this work, this transition temperature is approximately 100 K [85], far exceeding its experimental operating temperature. For a beam with a rectangular cross section, this boundary-limited mean free path is

given by  $\Lambda = 1.12\sqrt{wd}$ , where  $w$  and  $d$  are the width and thickness of the beam [86–90]. Inputting this relation, along with Eqs. (E2) and (E3), into Eq. (E1) allows us to express the boundary-limited thermal relaxation time as

$$\tau = \frac{3l^2}{1.12\pi^2 c_s \sqrt{wd}}. \quad (\text{E4})$$

Therefore, at low temperatures and for small cross sections ( $T \lesssim 100$  K for dimensions on the order of 100 nm [85]), the thermal relaxation time for a silicon beam depends only on the geometry and speed of sound of the system, which are to first order temperature-independent.

While the above description works well for determining the thermal time constant of a simple beam with a uniform rectangular cross section, it is unclear if such an analysis applies to the complex device structure studied here. Therefore, we have performed finite element simulations to accurately determine the thermal relaxation time for this device [41]. Here, the phonon mean free path is limited by the smallest dimension of our resonator (i.e.,  $w_3 = 151$  nm in Fig. 7), leading to  $\Lambda = 1.12\sqrt{w_3 d} = 218$  nm, where we have taken  $d = 250$  nm as the thickness of the silicon device. Using this value for the mean free path, along with the temperature-dependent expressions for the specific heat capacity and thermal conductivity found in Eqs. (E2) and (E3), we simulate the heating of the device due to absorption of laser power. To do this, the laser-driven heating is approximated as a uniform heat load applied to the inner surface of the resonator facing the disk [see inset of Fig. 16]. The magnitude of this heat load is chosen to be  $P_{\text{abs}} = 6 \mu\text{W}$  to approximately match the expected

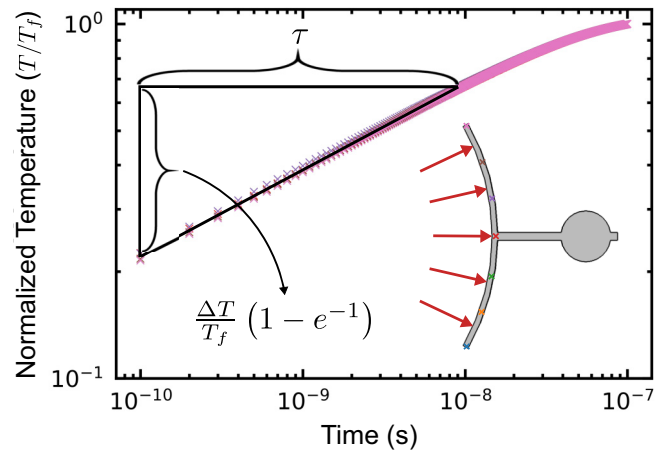


FIG. 16. Plot of the normalized temperature  $T/T_f$  versus time for the finite element heating simulation used to determine the thermal relaxation time of the resonator. Inset is a schematic illustrating the simulation procedure, whereby a uniform heat load of  $6 \mu\text{W}$  is applied to the surface of the resonator indicated by the red arrows, while its temperature profile is probed in time at the positions denoted by the colored crosses. By normalizing each of these extracted data sets (color-coded to match the corresponding probe point) to its final temperature, a universal heating trend along the curved portion of the resonator is demonstrated. From these normalized profiles, we determine the thermal relaxation time of the device ( $\tau = 9.5$  ns) as the time required for the temperature to increase from its initial value by an amount  $\Delta T(1 - e^{-1})$  [see Eq. (E5)].

absorbed power for the conditions associated with Fig. 4 (i.e.,  $\kappa = 2.04$  GHz,  $\kappa_e = 0.38$  GHz, and  $P_{\text{in}} = 10.1 \mu\text{W}$ ), while also assuming  $\kappa_a = \kappa_i$  and  $\Delta = 0$  (see Appendix B 6). The simulated temperature increase of the resonator as a function of time is then monitored at seven equally spaced points along its rounded portion, as shown in Fig. 16. Continuing with the Zener approximation (i.e., the majority of this thermal relaxation occurs through the fundamental mode of the resonator), we expect the temperature at each of these points to increase according to [29,83,91]

$$T(t) = T_0 + \Delta T(1 - e^{-t/\tau}). \quad (\text{E5})$$

Here  $\Delta T = T_f - T_0$  is the difference between the resonator's temperature  $T_0$  at  $t = 0$  when the heat load is initially applied and its final equilibrium temperature  $T_f$  that is reached for  $t \gg \tau$ . We note that while each point on the resonator heats from an initial temperature of  $T_0 = 4.2$  K to varying equilibrium temperatures ranging from  $T_f = 43$  K to  $T_f = 49$  K, when normalized by these final temperatures, each simulated data set collapses onto a single universal trace (see Fig. 16). Therefore, we can use Eq. (E5) to extract the thermal relaxation time

as the average time required for the resonator to heat from  $T_0$  to  $T_0 + \Delta T(1 - e^{-1})$ . Performing this calculation for each of these data sets, we find  $\tau = 9.5 \pm 0.2$  ns, where the uncertainty is given by the standard deviation of this distribution.

To conclude this section, we use this simulated value of  $\tau$  to evaluate how well our irregular resonator geometry is approximated as a uniform rectangular beam (with width  $w_3$  and thickness  $d$ ). This is done by rearranging Eq. (E4) to obtain an effective thermal length of

$$l_{\text{eff}} = \sqrt{\frac{1.12\pi^2 c_s \tau \sqrt{w_3 d}}{3}}. \quad (\text{E6})$$

Using the simulated time constant and the parameters for our device, we find this effective length to be  $l_{\text{eff}} = 6.24 \mu\text{m}$ . Comparing this value to the total length of our device,  $l_{\text{tot}} = l_1 + l_2 + l_3 + 2R_d = 7.06 \mu\text{m}$ , as measured from the tip of one end of the rounded portion of the resonator to its anchor point, we find that these two lengths agree very well with each other. Thus, our device is well-approximated as a uniform beam provided we introduce a small reduction in its length by a numerical factor of  $l_{\text{eff}}/l_{\text{tot}} = 0.88$ .

- 
- [1] J. D. Teufel, T. Donner, M. A. Castellanos-Beltran, J. W. Harlow, and K. W. Lehnert, *Nat. Nanotechnol.* **4**, 820 (2009).
- [2] A. G. Krause, M. Winger, T. D. Blasius, Q. Lin, and O. Painter, *Nat. Photon.* **6**, 768 (2012).
- [3] E. Gavartin, P. Verlot, and T. J. Kippenberg, *Nat. Nanotechnol.* **7**, 509 (2012).
- [4] P. H. Kim, B. D. Hauer, C. Doolin, F. Souris, and J. P. Davis, *Nat. Commun.* **7**, 13165 (2016).
- [5] T. A. Palomaki, J. W. Harlow, J. D. Teufel, R. W. Simmonds, and K. W. Lehnert, *Nature* **495**, 210 (2013).
- [6] R. Riedinger, S. Hong, R. A. Norte, J. A. Slater, J. Shang, A. G. Krause, V. Anant, M. Aspelmeyer, and S. Gröblacher, *Nature* **530**, 313 (2016).
- [7] A. P. Reed, K. H. Mayer, J. D. Teufel, L. D. Burkhardt, W. Pfaff, M. Reagor, L. Sletten, X. Ma, R. J. Schoelkopf, E. Knill, and K. W. Lehnert, *Nat. Phys.* **13**, 1163 (2017).
- [8] S. Bose, K. Jacobs, and P. L. Knight, *Phys. Rev. A* **59**, 3204 (1999).
- [9] W. Marshall, C. Simon, R. Penrose, and D. Bouwmeester, *Phys. Rev. Lett.* **91**, 130401 (2003).
- [10] O. Romero-Isart, A. C. Pflanzer, F. Blaser, R. Kaltenbaek, N. Kiesel, M. Aspelmeyer, and J. I. Cirac, *Phys. Rev. Lett.* **107**, 020405 (2011).
- [11] Y. Chen, *J. Phys. B* **46**, 104001 (2013).
- [12] I. Pikovski, M. R. Vanner, M. Aspelmeyer, M. S. Kim, and Č. Brukner, *Nat. Phys.* **8**, 393 (2012).
- [13] B. P. Abbott *et al.*, *Phys. Rev. Lett.* **116**, 061102 (2016).
- [14] C. Pfister, J. Kaniewski, M. Tomamichel, A. Mantri, R. Schmucker, N. McMahon, G. Milburn, and S. Wehner, *Nat. Commun.* **7**, 13022 (2016).
- [15] A. Belenchia, D. M. T. Benincasa, S. Liberati, F. Marin, F. Marino, and A. Ortolan, *Phys. Rev. Lett.* **116**, 161303 (2016).
- [16] M. Aspelmeyer, T. J. Kippenberg, and F. Marquardt, *Rev. Mod. Phys.* **86**, 1391 (2014).
- [17] A. A. Clerk and F. Marquardt, Basic theory of cavity optomechanics, in *Cavity Optomechanics: Nano- and Microelectromechanical Resonators Interacting with Light*, edited by M. Aspelmeyer, T. J. Kippenberg, and F. Marquardt (Springer, Berlin, 2014), Chap. 2.
- [18] J. D. Teufel, T. Donner, D. Li, J. W. Harlow, M. S. Allman, K. Cicak, A. J. Sirois, J. D. Whittaker, K. W. Lehnert, and R. W. Simmonds, *Nature* **475**, 359 (2011).
- [19] J. Chan, T. P. Mayer Alegre, A. H. Safavi-Naeini, J. T. Hill, A. Krause, S. Gröblacher, M. Aspelmeyer, and O. Painter, *Nature* **478**, 89 (2011).
- [20] T. A. Palomaki, J. D. Teufel, R. W. Simmonds, and K. W. Lehnert, *Science* **342**, 710 (2013).
- [21] R. Riedinger, A. Wallucks, I. Marinković, C. Löschnauer, M. Aspelmeyer, S. Hong, and S. Gröblacher, *Nature* **556**, 473 (2018).
- [22] C. F. Ockeloen-Korppi, E. Damskägg, J.-M. Pirkkalainen, M. Asjad, A. A. Clerk, F. Massel, M. J. Wooley, and M. A. Sillanpää, *Nature* **556**, 478 (2018).
- [23] E. E. Wollman, C. U. Lei, A. J. Weinstein, J. Suh, A. Kronwald, F. Marquardt, A. A. Clerk, and K. C. Schwab, *Science* **349**, 952 (2015).
- [24] J.-M. Pirkkalainen, E. Damskägg, M. Brandt, F. Massel, and M. A. Sillanpää, *Phys. Rev. Lett.* **115**, 243601 (2015).
- [25] M. Pinard and A. Danton, *New J. Phys.* **10**, 095012 (2008).
- [26] J. Restrepo, J. Gabelli, C. Ciuti, and I. Favero, *C. R. Physique* **12**, 860 (2011).
- [27] S. De Liberato, N. Lambert, and F. Nori, *Phys. Rev. A* **83**, 033809 (2011).
- [28] M. Abdi and A. R. Bahrapour, *Phys. Rev. A* **85**, 063839 (2012).
- [29] M. Abdi, A. R. Bahrapour, and D. Vitali, *Phys. Rev. A* **86**, 043803 (2012).

- [30] J. Mertz, O. Marti, and J. Mlynek, *Appl. Phys. Lett.* **62**, 2344 (1993).
- [31] M. Vogel, C. Mooser, K. Karrai, and R. J. Warburton, *Appl. Phys. Lett.* **83**, 1337 (2003).
- [32] C. Höhberger Metzger and K. Karrai, *Nature* **432**, 1002 (2004).
- [33] C. Metzger, I. Favero, A. Ortlieb, and K. Karrai, *Phys. Rev. B* **78**, 035309 (2008).
- [34] C. Metzger, M. Ludwig, C. Neuenhahn, A. Ortlieb, I. Favero, K. Karrai, and F. Marquardt, *Phys. Rev. Lett.* **101**, 133903 (2008).
- [35] G. Jourdan, F. Comin, and J. Chevrier, *Phys. Rev. Lett.* **101**, 133904 (2008).
- [36] J. G. E. Harris, B. M. Zwickl, and A. M. Jayich, *Rev. Sci. Instrum.* **78**, 013107 (2007).
- [37] I. Favero, C. Metzger, S. Camerer, D. König, H. Lorenz, J. P. Kotthaus, and K. Karrai, *Appl. Phys. Lett.* **90**, 104101 (2007).
- [38] K. Aubin, M. Zalalutdinov, T. Alan, R. B. Reichenbach, R. Rand, A. Zehnder, J. Parpia, and H. Craighead, *J. Microelectromech. Syst.* **13**, 1018 (2004).
- [39] D. Yuvaraj, M. B. Kadam, O. Shtempluck, and E. Buks, *J. Microelectromech. Syst.* **22**, 430 (2012).
- [40] S. Gigan, H. R. Böhm, M. Paternostro, F. Blaser, G. Langer, J. B. Hertzberg, K. C. Schwab, D. Bäuerle, M. Aspelmeyer, and A. Zeilinger, *Nature* **444**, 67 (2006).
- [41] M. W. Pruessner, T. H. Stievater, J. B. Khurgin, and W. S. Rabinovich, *Opt. Express* **19**, 21904 (2011).
- [42] K. Usami, A. Naesby, T. Bagci, B. Melholt Nielsen, J. Liu, S. Stobbe, P. Lodahl, and E. S. Polzik, *Nat. Phys.* **8**, 168 (2012).
- [43] A. Xuereb, K. Usami, A. Naesby, E. S. Polzik, and K. Hammerer, *New J. Phys.* **14**, 085024 (2012).
- [44] R. A. Barton, I. R. Storch, V. P. Adiga, R. Sakakibara, B. R. Cipriany, B. Ilic, S. P. Wang, P. Ong, P. L. McEuen, J. M. Parpia, and H. G. Craighead, *Nano. Lett.* **12**, 4681 (2012).
- [45] S. Zaitsev, A. K. Pandey, O. Shtempluck, and E. Buks, *Phys. Rev. E* **84**, 046605 (2011).
- [46] M. Hosseini, G. Guccione, H. J. Slatyer, B. C. Buchler, and P. K. Lam, *Nat. Commun.* **5**, 4663 (2014).
- [47] R. De Alba, T. S. Abhilash, R. H. Rand, H. G. Craighead, and J. M. Parpia, *Nano. Lett.* **17**, 3995 (2017).
- [48] C. Belacel, Y. Todorov, S. Barbieri, D. Gacemi, I. Favero, and C. Sirtori, *Nat. Commun.* **8**, 1578 (2017).
- [49] G. I. Harris, D. L. McAuslan, E. Sheridan, Y. Sachkou, C. Baker, and W. P. Bowen, *Nat. Phys.* **12**, 788 (2016).
- [50] A. D. Kashkanova, A. B. Shkarin, C. D. Brown, N. E. Flowers-Jacobs, L. Childress, S. W. Hoch, L. Hohmann, K. Ott, J. Reichel, and J. G. E. Harris, *Nat. Phys.* **13**, 74 (2017).
- [51] A. D. Kashkanova, A. B. Shkarin, C. D. Brown, N. E. Flowers-Jacobs, L. Childress, S. W. Hoch, L. Hohmann, K. Ott, J. Reichel, and J. G. E. Harris, *J. Opt.* **19**, 034001 (2017).
- [52] F. Marquardt, J. G. E. Harris, and S. M. Girvin, *Phys. Rev. Lett.* **96**, 103901 (2006).
- [53] M. Ludwig, B. Kubala, and F. Marquardt, *New J. Phys.* **10**, 095013 (2008).
- [54] A. G. Krause, J. T. Hill, M. Ludwig, A. H. Safavi-Naeini, J. Chan, F. Marquardt, and O. Painter, *Phys. Rev. Lett.* **115**, 233601 (2015).
- [55] F. M. Buters, H. J. Eerkens, K. Heeck, M. J. Weaver, B. Pepper, S. de Man, and D. Bouwmeester, *Phys. Rev. A* **92**, 013811 (2015).
- [56] J. D. Cohen, S. M. Meenehan, G. S. MacCabe, S. Gröblacher, A. H. Safavi-Naeini, F. Marsili, M. D. Shaw, and O. Painter, *Nature* **520**, 522 (2015).
- [57] S. Hong, R. Riedinger, I. Marinković, A. Wallucks, S. G. Hofer, R. A. Norte, M. Aspelmeyer, and S. Gröblacher, *Science* **358**, 203 (2017).
- [58] I. Marinković, A. Wallucks, R. Riedinger, S. Hong, M. Aspelmeyer, and S. Gröblacher, *Phys. Rev. Lett.* **121**, 220404 (2018).
- [59] A. Schliesser, R. Rivière, G. Anetsberger, O. Arcizet, and T. J. Kippenberg, *Nat. Phys.* **4**, 415 (2008).
- [60] B. D. Hauer, C. Doolin, K. S. D. Beach, and J. P. Davis, *Ann. Phys.* **339**, 181 (2013).
- [61] A. J. R. MacDonald, G. G. Popowich, B. D. Hauer, P. H. Kim, A. Fredrick, X. Rojas, P. Doolin, and J. P. Davis, *Rev. Sci. Instrum.* **86**, 013107 (2015).
- [62] C. P. Michael, M. Borselli, T. J. Johnson, C. Chrystal, and O. Painter, *Opt. Express* **15**, 4745 (2007).
- [63] B. D. Hauer, P. H. Kim, C. Doolin, A. J. R. MacDonald, H. Ramp, and J. P. Davis, *EPJ Tech. Instrum.* **1**, 4 (2014).
- [64] B. D. Hauer, P. H. Kim, C. Doolin, F. Souris, and J. P. Davis, *Phys. Rev. B* **98**, 214303 (2018).
- [65] R. Lifshitz and M. C. Cross, Nonlinear dynamics of nanomechanical and micromechanical resonators, in *Review of Nonlinear Dynamics and Complexity*, edited by H. G. Schuster (Wiley, Weinheim, 2008), Vol. 1, Chap. 1.
- [66] K. G. Lyon, G. L. Salinger, C. A. Swenson, and G. K. White, *J. Appl. Phys.* **48**, 865 (1977).
- [67] T. Carmon, L. Yang, and K. J. Vahala, *Opt. Express* **12**, 4742 (2004).
- [68] A. J. R. MacDonald, B. D. Hauer, X. Rojas, P. H. Kim, G. G. Popowich, and J. P. Davis, *Phys. Rev. A* **93**, 013836 (2016).
- [69] F. Marquardt, J. P. Chen, A. A. Clerk, and S. M. Girvin, *Phys. Rev. Lett.* **99**, 093902 (2007).
- [70] F. Elste, S. M. Girvin, and A. A. Clerk, *Phys. Rev. Lett.* **102**, 207209 (2009).
- [71] A. Xuereb, R. Schnabel, and K. Hammerer, *Phys. Rev. Lett.* **107**, 213604 (2011).
- [72] F. Marino and F. Marin, *Phys. Rev. E* **83**, 015202(R) (2011).
- [73] F. Marino and F. Marin, *Phys. Rev. E* **87**, 052906 (2013).
- [74] B. D. Hauer, J. Maciejko, and J. P. Davis, *Ann. Phys.* **361**, 148 (2015).
- [75] A. A. Clerk, M. H. Devoret, S. M. Girvin, F. Marquardt, and R. J. Schoelkopf, *Rev. Mod. Phys.* **82**, 1155 (2010).
- [76] M. L. Gorodetsky, A. Schliesser, G. Anetsberger, S. Deleglise, and T. J. Kippenberg, *Opt. Express* **18**, 23236 (2010).
- [77] T. Carmon, H. Rokhsari, L. Yang, T. J. Kippenberg, and K. J. Vahala, *Phys. Rev. Lett.* **94**, 223902 (2005).
- [78] T. J. Kippenberg, H. Rokhsari, T. Carmon, A. Scherer, and K. J. Vahala, *Phys. Rev. Lett.* **95**, 033901 (2005).
- [79] H. Rokhsari, T. J. Kippenberg, T. Carmon, and K. J. Vahala, *Opt. Express* **13**, 5293 (2005).
- [80] M. Ludwig, Ph.D. thesis, Friedrich-Alexander University Erlangen-Nürnberg, 2013.
- [81] C. Zener, *Elasticity and Anelasticity of Metals* (University of Chicago Press, Chicago, 1948).
- [82] R. Lifshitz and M. L. Roukes, *Phys. Rev. B* **61**, 5600 (2000).
- [83] M. W. Pruessner, T. H. Stievater, M. S. Ferraro, and W. S. Rabinovich, *Opt. Express* **15**, 7557 (2007).

- [84] F. Pobell, *Matter and Methods at Low Temperatures* (Springer-Verlag, Berlin, 2007).
- [85] L. Weber and E. Gmelin, *Appl. Phys. A* **53**, 136 (1991).
- [86] H. B. G. Casimir, *Physica* **5**, 495 (1938).
- [87] J. M. Ziman, *Electrons and Phonons: The Theory of Transport Phenomena in Solids* (Oxford University Press, Oxford, 2001).
- [88] J. S. Heron, T. Fournier, N. Mingo, and O. Bourgeois, *Nano Lett.* **9**, 1861 (2009).
- [89] J.-S. Heron, C. Bera, T. Fournier, N. Mingo, and O. Bourgeois, *Phys. Rev. B* **82**, 155458 (2010).
- [90] D. G. Cahill, P. V. Braun, G. Chen, D. R. Clark, S. Fan, K. E. Goodson, P. Keblinski, W. P. King, G. D. Mahan, A. Majumdar, H. J. Maris, S. R. Phillpot, E. Pop, and L. Shi, *Appl. Phys. Rev.* **1**, 011305 (2014).
- [91] H. S. Carslaw and J. C. Jaeger, *Conduction of Heat in Solids* (Oxford University Press, Oxford, 1959).